

COMPUTATIONAL SIMULATION OF RHEOLOGICAL BLOOD FLOW CONTAINING HYBRID NANOPARTICLES IN AN INCLINED CATHETERIZED ARTERY WITH STENOTIC, ANEURYSMAL AND SLIP EFFECTS**Jayati Tripathi¹, B. Vasu^{1*}, O. Anwar Bég², Rama Subba Reddy Gorla³ and Peri K. Kameswaran⁴**¹Department of Mathematics, Motilal Nehru National Institute of Technology Allahabad, Prayagraj-211004 U.P., **India**.²MPESG, Department of Mechanical Engineering, Salford University, Salford, M54WT, **UK**,³Department of Aeronautics and Astronautics, Air Force Institute of Technology, Wright Patterson Air Force Base, Dayton, Ohio 45433, **USA**⁴Department of Mathematics, School of Advanced Sciences, VIT University, Vellore 632014, **India**

Abstract: Influenced by nano-drug delivery applications, the present article considers the collective effects of hybrid biocompatible metallic nanoparticles (Silver and Copper), a stenosis and an aneurysm on the unsteady blood flow characteristics in a catheterized tapered inclined artery. The non-Newtonian Carreau fluid model is deployed to represent the hemorheological characteristics in the arterial region. A modified Tiwari-Das volume fraction model is adopted for nanoscale effects. The permeability of the arterial wall and the inclination of the diseased artery are taken into account. The nanoparticles are also considered to have various shapes (bricks, cylinders, platelets, blades) and therefore the influence of different shape parameters is discussed. The conservation equations for mass, linear momentum and energy are normalized by employing suitable non-dimensional variables. The transformed equations with associated boundary conditions are solved numerically using the FTCS method. Key hemodynamic characteristics i.e. velocity, temperature, flow rate, wall shear stress (WSS) in stenotic and aneurysm region for a particular critical height of the stenosis, are computed. Hybrid nanoparticles (Ag-Cu/Blood) accelerate the axial flow and increase temperatures significantly compared with unitary nanoparticles (Ag/blood), at both the stenosis and aneurysm segments. Axial velocity, temperature and flow rate are all enhanced with greater nanoparticle shape factor. Axial velocity, temperature, wall shear stress and flow rate magnitudes are always comparatively higher at the aneurysm region compared with the stenotic segment. The simulations provide novel insights into the performance of different nanoparticle geometries and also rheological behaviour in realistic nano-pharmaco-dynamic transport and percutaneous coronary intervention (PCI).

Keywords: *Mild stenosis, aneurysm, non-Newtonian (Carreau) fluid, catheterized artery, blood flow, hybrid nanofluid, nanoparticle shape factor, wall slip, inclined artery, wall permeability*

Nomenclature

B_1	Pressure gradient parameter
C_p	Heat capacitance
Fr	Froude number
Gr	Grashof number
k	Thermal conductivity
l_i	Length of diseased segment
m	$m = \frac{\mu_\infty}{\mu_0}$, i.e. ratio of dynamic viscosity (μ_0) and infinite shear-rate viscosity (μ_∞)
n	non-Newtonian power law index in Carreau model
n_2	Nanoparticle shape parameter
Pr	Prandtl number
p	Pressure
Q	Flow rate
r	Radial co-ordinate
R	Radius of the artery (stenotic)
R_0	Radius of the artery (non-stenotic)
Re	Reynolds number
t	Time
T	Temperature
u	Radial velocity
w	Axial velocity
z	Axial co-ordinate

Greek Letters

θ	Dimensionless temperature
α	Distance of diseased segment from origin
β	Heat generation parameter
μ_0	Reference dynamic viscosity in Carreau model
μ_∞	Infinite shear-rate viscosity in Carreau model
λ	Inclination angle
ρ	Density
ϕ	Tapering angle
ϕ_1, ϕ_2	Nanoparticle concentration
δ	Depth of stenosis
γ	Thermal expansion coefficient
τ	Wall shear stress

1. Introduction:

The study of hemodynamics in stenosed or aneurysmal arteries is a critical area of interest owing to many significant applications in cardiovascular diseases such as atherosclerosis, aneurysms, angina, or heart attacks which are among the leading causes of deaths worldwide. Cardiovascular diseases often arise in coronary arteries and are associated with depositing fatty substances inside the arterial wall lumen. This process decreases the blood vessel radius while enhancing the resistance (impedance) to blood flow, thereby effectively inhibiting the supply of oxygenated blood from the heart to other parts of the human body. Hence the formation of stenosis continually advances with time to manifest as serious circulatory and arterial diseases. Mainly, with the help of laboratory investigations, complementary numerical simulations are constructive in treating cardiovascular diseases.

Several studies have been conducted theoretically and experimentally to understand the exact mechanisms of stenosis development and its influence on blood flow characteristics. It is noted that hemodynamics in the post-stenotic regions is linked with the development and continuation of stenosis. Rindfleish [1] and Nazemi et al. [2] noted that wall shear stress is a key factor in the progression of stenotic lesions. Fry [3] observed that high wall shear stress is a principal contributor to endothelial cell damage. It is also known that the formation of stenosis alters the flow characteristics in its vicinity. The hemodynamics can be categorized according to the geometry of the arterial segment. For medical engineering purposes, a rigid cylindrical tube with a single symmetric and non-symmetric hindrance is the most familiar model deployed in a stenotic arterial segment simulation. Many biomedical engineers and scientists have used this model to understand the blood flow characteristics in the stenosed arteries [4-7]. However, it is possible for stenoses to have irregular shapes or not be in series. Studies related to the multiple, irregular, or overlapped stenoses in an artery are available in refs. [8-10]. Moore [11] emphasized that multiple stenoses and post-stenotic dilatations are found to be very common in the coronary arteries. Many investigations have confirmed that non-Newtonian models provide much greater accuracy in representing the actual characteristics (rheological) of blood (particularly in smaller blood vessels) and that a high/low shear rate cycle exists within the cardiac period of heart pumping. Among various non-Newtonian models, which include viscoelastic (e.g., Oldroyd-B), viscoplastic (Casson), short memory (Walters-B), and microstructural (polar, micropolar, micro stretch)

formulations, the Carreau fluid model (and its modifications) is the most amenable approach for representing hemodynamic phenomena over different shear rates. Gijsen et al. [12] presented a numerical investigation of blood flow in 90° curved tubes using the Carreau-Yasuda model, elaborating the relative performance, for small Reynolds numbers, of both Newtonian and non-Newtonian behavior. Other hemorheological stenotic and post-stenotic blood flow studies include Manica and Bortoli [13], who computed both incompressible Newtonian and non-Newtonian (pseudoplastic/dilatant) blood flow through channels. Pincombe and Mazumbar [14] used the Casson model. Additionally, Ali et al. [15] studied the blood flow in a w-shaped stenotic arterial segment with the Oldroyd-B viscoelastic model. All these studies confirmed the significant contribution of rheological behavior in modifying hemodynamic characteristics, particularly downstream of the stenotic zone.

Blood flow through arteries becomes more complicated due to the development of an aneurysm. An aneurysm is like balloon dilation found on the arterial wall, usually noticed in carotid, abdominal, cerebral, and femoral arteries. It slowly increases in starting, but later the progression is seen rapidly with time. Ali et al. [16] presented one of the first stenotic/aneurysm hemodynamic computational simulations using the Eringen micropolar model, also considering a tapered catheterized arterial region. Several other studies [17-18] have highlighted the importance of hemodynamics in aneurysm formation. Sharzehee et al. [19] employed fluid-structure interaction (FSI) modeling in pulsatile blood flow through a diseased artery with aneurysm and included a hydrodynamic stability analysis, demonstrating that aneurismal arteries are more susceptible than normal arteries to instability.

In medicine, catheterization is an effective procedure utilized in treating haematological disorders such as atherosclerosis. It involves deploying a long, thin, and flexible tube (catheter) inserted in a stenotic blood vessel. The insertion of the catheter into a diseased artery forms an annular region between the catheter wall and vascular wall, which aims to improve the hemodynamic conditions in the artery [20]. Mekheimer et al. [21] analyzed the two-phase (fluid-particle suspension) blood flow through a catheterized stenotic overlapping artery, including heat transfer and entropy generation. Ahmed and Nadeem [22] studied the copper nanoparticle-doped blood flow through a curved catheterized artery containing a balloon angioplasty and included nanoparticle shape effects. An essential feature of real arteries is the permeability of the blood vessel. This property

permits the diffusion of oxygen and other vital nutrients through the vessel into the streaming blood flow, thereby enabling the distribution of essential substances to the entire cardiovascular system. Bali and Awasthi [23] presented a detailed analysis of the hemodynamic flow through a composite artery with a porous wall, also considering Newtonian blood flow characteristics. Srivastav [24] studied the Newtonian blood flow through composite stenosis in catheterized artery with a permeable wall. Further studies addressing the permeability effect for various stenotic geometries have been communicated by Singh et al. [25], Akbar et al. [26], and Eldesoky [27].

In recent decades, nanofluids have emerged as a significant development in biomedical engineering. Choi [28] proposed the term "nanofluid," which constitutes a suspension of dissimilar nanoparticles suspended in a base fluid, aimed at elevating overall thermal characteristics. It has been confirmed clinically that the inclusion of nanoparticles in the base fluid, e.g. blood, increases the thermal conductivity by a remarkable degree. Among numerous nanotechnology applications in modern medicine, drug delivery (pharmacodynamics) has enabled clinicians and pharmacists to bring significant improvement in healthcare at the molecular level. Tripathi et al. [29] conducted a detailed review of the recent hemodynamic nano-drug delivery systems advancements. Theoretical and numerical studies pertaining to nanofluid applications in biomedicine include [30-33]. However, the studies mentioned above were restricted to the consideration of a single type of nanoparticle material in hemodynamics. This is known as the unitary nanofluid, i.e., blood doped with a single nanoparticle material type. However, Makishima et al. [34] suggested nanofluid suspensions comprising two or more compatible nanoparticles dispersed in a base fluid to provide a homogenous mixture, i.e., hybrid nanofluids. Compared with unitary nanofluid, hybrid nanofluid successfully combines the unique individual thermophysical properties of multiple nanoparticles, which offers significant advantages in improving medical results. Tripathi et al. [35] examined theoretically, and numerically the unsteady blood flow doped with hybrid nanoparticles (gold and silver) through a diseased artery having irregular stenosis as a simulation of nano-pharmacological transport. Zaman et al. [36] simulated the hybrid nanoparticles (copper and silver) doped blood flow through a curved stenosed artery having an aneurysm, employing a forward time centered space (FTCS) method. Similarly, Tripathi et al. [37] performed a study for unsteady hybrid (gold-silver) mediated nanoparticle-doped biomagnetic blood flow and heat transport in a diseased artery featuring an overlapped stenosis. They showed that hybrid nanoparticle-doped blood produces more beneficial results for nano-drug delivery therapies.

With the motivation of these above-mentioned studies, in the present investigation, a novel mathematical model is developed to simulate the *effects of different shaped (brick, cylinder, platelet and blades) hybrid (Ag+Cu) nanoparticles in the pharmacodynamic transport with wall slip in an inclined catheterized tapered artery featuring both a mild stenosis and aneurysm*. To represent the non-Newtonian characteristics of blood, the Carreau rheological (shear-thinning) model is applied. In addition, the slip velocity and pulsatile pressure gradient effects are implemented to provide a more realistic representation of actual blood flows under unsteady flow conditions. Heat generation effect and the permeability of blood vessel are also included. A modified Tiwari-Das volume fraction model is adopted for nanoscale effects. Consequently, to the best of the author's knowledge the *computation of different shaped hybrid nanoparticles (Ag+Cu) in rheological hemodynamics through a catheterized tapered inclined blood vessel having a mild stenosis and aneurysm and with arterial wall permeability, hydrodynamic slip and internal heat generation*, has not been explored yet in biomedical computational fluid dynamics; this constitutes the novelty of the present article. With appropriate boundary conditions, the normalized (non-dimensional) non-linear conservation equations are solved by an efficient finite difference method (FTCS). Further simulations and visualizations are produced in MATLAB software. The remainder of the article is divided into the following sections: Section 2 illustrates the arterial geometry of model (for mild stenosis and aneurysm) with associated geometric formulations. Section 3 explains the mathematical formulation based on the hybrid nanofluid model and elaborates on the partial differential conservation equations (mass, momentum and energy) and boundary conditions. In section 4, non-dimensionalization of the boundary value problem is performed, which permits the introduction of key scaling parameters i.e., Reynolds number, Prandtl number, Froude number, Darcy number etc. Section 5 provides a detailed explanation of FTCS numerical technique. Section 6 presents a comprehensive validation of problem. Section 7 contains all the results and physical interpretation for the impact of selected parameters e. g. nanoparticle concentration (volume fraction) on *velocity, temperature, wall shear stress and volumetric flow rate*. Lastly, in section 8, the principal findings of the study are summarized with some pathways suggested for future work in nano-pharmacological hemodynamics.

2. Arterial geometry for stenotic/aneurismal flow model:

Blood flow is considered to be axisymmetric, laminar, incompressible and unsteady in nature. The mathematical equations describing the geometry are formulated in a cylindrical co-ordinate system $(\bar{r}, \bar{\theta}, \bar{z})$, in which \bar{r} is radial coordinate, $\bar{\theta}$ is circumferential (tangential) coordinate and \bar{z} is axial co-ordinate, respectively. Since the flow is considered here as axisymmetric, hence the circumferential direction is neglected. The physical model is visualized in **Fig. 1**. Further, the mathematical expression of mild stenosis [38] in an artery is presented as:

$$R(z) = \left\{ \begin{array}{ll} \left[(m_1 z + R_0) - \frac{\delta_i}{2R_0} \left(1 + \cos \frac{2\pi}{l_i} \left(z - \alpha_i - \frac{l_i}{2} \right) \right) \right], & \alpha_i \leq z \leq \alpha_i + l_i, \\ (m_1 z + R_0), & \text{otherwise} \end{array} \right\} \quad (1)$$

In the above expression, $R(z)$ is defined as the radius of diseased segment, α_i represents the distance of the abnormal section from the origin, R_0 denotes the radius of the normal artery, δ_i as the maximum height of the stenosis and l_i is the length of abnormal section. Here $m_1 = \tan \phi$ is the *slope* the tapered artery. The possibility of different shapes of the artery is explored by considering a *convergent* artery when $\phi < 0$ and a *divergent* artery when $\phi > 0$. Here the radius of catheter is considered as R_c . Inclination of the artery invokes *gravitational effects* which are important in providing a more realistic appraisal of actual hemodynamics.

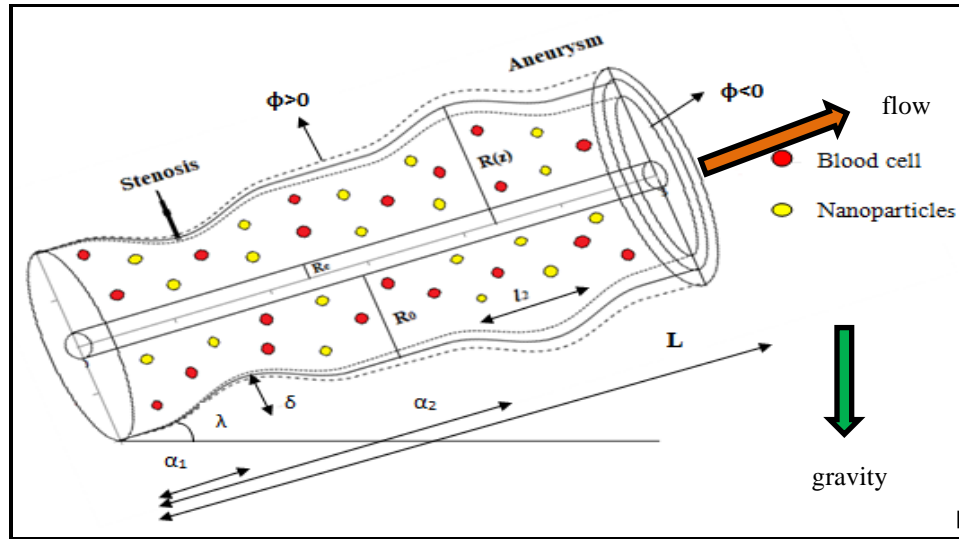


Figure 1: Physical model for hybrid nanoparticle-doped hemodynamics in a stenotic and aneurismal inclined catheterized tapered artery

3. Mathematical transport model for hybrid nanoparticle-doped blood flow:

For the unsteady and axisymmetric hybrid nanofluid blood flow model, the velocity and temperature profile for the current problem are defined as follows:

$$V = [u(r, z, t), 0, w(r, z, t)]$$

$$T = T(r, z, t) \quad (2)$$

where u and w are the radial and axial velocity components, respectively. In view of above equation and considering the hybrid nanoparticles model, the equation of continuity, momentum, and energy can be written as [39]:

$$\frac{\partial u}{\partial r} + \frac{u}{r} + \frac{\partial w}{\partial z} = 0 \quad (3)$$

$$\rho_{hmf} \left[\frac{\partial w}{\partial t} + u \frac{\partial w}{\partial r} + w \frac{\partial w}{\partial z} \right] = -\frac{\partial p}{\partial z} + \left[\frac{1}{r} \frac{\partial}{\partial r} (r S^{rz}) + \frac{\partial}{\partial z} (S^{zz}) \right] + (\rho\gamma)_{hmf} g (T - T_1) \sin \lambda + \rho_{hmf} g \sin \lambda \quad (4)$$

$$\rho_{hmf} \left[\frac{\partial u}{\partial t} + u \frac{\partial u}{\partial r} + w \frac{\partial u}{\partial z} \right] = -\frac{\partial p}{\partial r} + \left[\frac{1}{r} \frac{\partial}{\partial r} (r S^{rr}) + \frac{\partial}{\partial z} (S^{rz}) \right] - (\rho\gamma)_{hmf} g (T - T_1) \cos \lambda - \rho_{hmf} g \cos \lambda \quad (5)$$

$$\left[\frac{\partial T}{\partial t} + u \frac{\partial T}{\partial r} + w \frac{\partial T}{\partial z} \right] = \frac{k_{hmf}}{(\rho C_p)_{hmf}} \left[\frac{\partial^2 T}{\partial r^2} + \frac{1}{r} \frac{\partial T}{\partial r} + \frac{\partial^2 T}{\partial z^2} \right] + \frac{\beta}{(\rho C_p)_{hmf}} \quad (6)$$

The physical parameters that emerge in the above set of equations are defined as follows: ρ_{hmf} is the density of hybrid nanofluid (i.e. blood combined with hybrid nanoparticles), μ_{hmf} is the dynamic viscosity, γ_{hmf} is the thermal expansion coefficient, k_{hmf} is thermal conductivity, $(C_p)_{hmf}$ is the specific heat at constant pressure for the hybrid nanofluid model, λ is the inclination angle of the artery to the horizontal plane, β_o is the heat generation parameter. The terms S_{rr} , S_{rz} and S_{zz} appearing in Eqns. (4) and (5) are the component of extra stress. The constitutive equation for the Carreau rheological model is given as [40]:

$$S = \left(\mu_\infty + (\mu_0 + \mu_\infty) \left(1 + (\lambda \Pi)^2 \right)^{\frac{n-1}{2}} \right) A_1 \quad (7)$$

In Eqn. (7), μ_0 and μ_∞ are the dynamic and infinite shear-rate viscosities of blood. The parameter n represents the power law index, λ represents the time constant and A_1 represents the first Rivlin-Ericksen tensor as given below [40]:

$$A_1 = \Delta V + \Delta V^T \quad (8)$$

The second invariant of the first Rivlin-Ericksen tensor, Π , is defined as:

$$\Pi = \sqrt{\frac{1}{2} \text{tra}(A_1^2)} \quad (9)$$

In view of Eqn. (4), the constitutive relation (7) yields:

$$S^{rr} = 2 \left[\mu_\infty + (\mu_0 + \mu_\infty) \left\{ 1 + \lambda^2 \left[2 \left(\left(\frac{\partial u}{\partial r} \right)^2 + \left(\frac{u}{r} \right)^2 \right) + \left(\frac{\partial w}{\partial z} \right)^2 + \left(\frac{\partial u}{\partial z} + \frac{\partial w}{\partial r} \right)^2 \right] \right\}^{\frac{n-1}{2}} \right] \left(\frac{\partial u}{\partial r} \right) \quad (10)$$

$$S^{zz} = 2 \left[\mu_\infty + (\mu_0 + \mu_\infty) \left\{ 1 + \lambda^2 \left[2 \left(\left(\frac{\partial u}{\partial r} \right)^2 + \left(\frac{u}{r} \right)^2 \right) + \left(\frac{\partial w}{\partial z} \right)^2 + \left(\frac{\partial u}{\partial z} + \frac{\partial w}{\partial r} \right)^2 \right] \right\}^{\frac{n-1}{2}} \right] \left(\frac{\partial w}{\partial z} \right) \quad (11)$$

$$S^{rz} = \left[\mu_\infty + (\mu_0 + \mu_\infty) \left\{ 1 + \lambda^2 \left[2 \left(\left(\frac{\partial u}{\partial r} \right)^2 + \left(\frac{u}{r} \right)^2 \right) + \left(\frac{\partial w}{\partial z} \right)^2 + \left(\frac{\partial u}{\partial z} + \frac{\partial w}{\partial r} \right)^2 \right] \right\}^{\frac{n-1}{2}} \right] \left(\frac{\partial w}{\partial r} + \frac{\partial u}{\partial z} \right) \quad (12)$$

For the velocity profile and temperature field, the associated boundary and initial conditions are prescribed as follows for the arterial wall ($r=R$) and at the wall of catheter ($r=R_c$). The conditions also include a *hydrodynamic axial slip velocity* (w_B) at the vessel wall.

$$w(r,t)|_{r=R} = w_B, \quad T(r,t)|_{r=R} = T_w, \quad w(r,t)|_{r=R_c} = 0, \quad T(r,t)|_{r=R_c} = 0 \quad (13)$$

$$w(r,0) = 0, \quad T(r,0) = 0 \quad (14)$$

$$\frac{\partial w}{\partial r} = \frac{\alpha}{\sqrt{Da}} [w_B - w_{porous}] \quad (15)$$

In the boundary equation, Da presents the Darcy number (a dimensionless permeability parameter characterizing the porous nature of the vessel wall), α is defined as dimensionless slip parameter, w_B is the slip velocity and w_{porous} as the velocity of permeable boundary [48]. According to Darcy

$$\text{law, } w_{porous} \text{ is given by: } w_{porous} = -Da \left(\frac{dP}{dz} \right) \quad (16)$$

4. Non-dimensionalization of hybrid nanofluid model:

The mathematical model defined by Eqns. (3)-(6) can be made dimensionless with the help of the following set of parameters [39]:

$$\begin{aligned} \bar{r} &= \frac{r}{R_0}, \quad \bar{w} = \frac{w}{U_0}, \quad \bar{z} = \frac{z}{\tilde{L}}, \quad \bar{R} = \frac{R}{R_0}, \quad \bar{u} = \frac{\tilde{L}u}{\tilde{\delta}^*U_0}, \quad \bar{t} = \frac{U_0 t}{R_0}, \quad \bar{p} = \frac{R_0^2 p}{U_0 \tilde{L} \mu_0}, \quad \theta = \frac{T - T_1}{T_w - T_1}, \quad m = \frac{\mu_\infty}{\mu_0}, \\ \beta &= \frac{R_0^2 \beta_0}{(T_w - T_1) k_f}, \quad \text{Pr} = \frac{C_p \mu_0}{k_f}, \quad Gr = \frac{\rho_f \gamma_f g R_0^2 (T_w - T_1)}{\mu_0 U_0}, \quad \text{Re} = \frac{\rho_f U_0 R_0}{\mu_0}, \quad \bar{w}_B = \frac{w_B}{U_0}, \quad \overline{S^{zz}} = \frac{\tilde{L}}{U_0 \mu_0} S^{zz}, \\ \overline{S^{rr}} &= \frac{\tilde{L}}{U_0 \mu_0} S^{rr}, \quad \overline{S^{rz}} = \frac{R_0}{U_0 \mu_0} S^{rz}, \quad Fr = \frac{U_0^2}{g R_0}, \quad \gamma = \lambda \left(\frac{U_0}{R_0} \right)^{n-1} \end{aligned} \quad (17)$$

Here \bar{r} presents the dimensionless radial coordinate, \bar{w} is the dimensionless axial velocity, \bar{R} is dimensionless radius, \bar{z} is dimensionless axial coordinate, \bar{u} is dimensionless radial velocity component, \bar{t} is dimensionless time, \bar{p} is dimensionless pressure, θ is dimensionless blood temperature, β is dimensionless heat generation parameter and \bar{w}_B is dimensionless slip velocity.

In addition to this, Pr is the Prandtl number, Re is the Reynolds number, Gr is the local thermal Grashof number (ratio of thermal buoyancy force to viscous force) and Fr is the Froude number (ratio of inertial force to gravity force). U_0 appears as a reference velocity of blood flow and T_w is wall temperature. Here $\tilde{\delta}^*$ represents as $\tilde{\delta}^* = \max(\delta_1, \delta_2)$, and $\tilde{L} = \min(L_1, L_2)$. In the above-defined variables, the non-dimensional geometric parameters are *stenosis height parameter* ($\delta = \tilde{\delta}^*/R_0$) and *vessel aspect ratio* ($\varepsilon = R_0/\tilde{L}$).

Introducing the above-defined variables in Eqns. (3)-(6) and after dropping the bars, the following non-dimensional conservation equations for mass, momentum (axial and radial) and energy emerge:

$$\delta \left[\frac{\partial u}{\partial r} + \frac{u}{r} \right] + \frac{\partial w}{\partial z} = 0 \quad (18)$$

$$\begin{aligned} \left(\frac{\rho_{hmf}}{\rho_f} \right) \text{Re} \left[\frac{\partial w}{\partial t} + \delta \varepsilon u \frac{\partial w}{\partial r} + \varepsilon w \frac{\partial w}{\partial z} \right] = -\frac{\partial p}{\partial z} + \left[\frac{1}{r} \frac{\partial}{\partial r} (r S^{rz}) + \varepsilon^2 \frac{\partial}{\partial z} (S^{zz}) \right] + \frac{(\rho\gamma)_{hmf}}{(\rho\gamma)_f} \sin \lambda Gr(\theta) \\ + \frac{\rho_{hmf}}{\rho_f} \frac{\text{Re}}{Fr} \sin \lambda \end{aligned} \quad (19)$$

$$\begin{aligned} \left(\frac{\rho_{hmf}}{\rho_f} \right) \text{Re} \delta \varepsilon^2 \left[\frac{\partial u}{\partial t} + \delta \varepsilon u \frac{\partial u}{\partial r} + \varepsilon w \frac{\partial u}{\partial z} \right] = -\frac{\partial p}{\partial r} + \left[\varepsilon^2 \frac{1}{r} \frac{\partial}{\partial r} (r S^{rr}) + \varepsilon^2 \frac{\partial}{\partial z} (S^{rz}) \right] - \varepsilon \frac{(\rho\gamma)_{hmf}}{(\rho\gamma)_f} \cos \lambda Gr(\theta) \\ - \varepsilon \frac{\rho_{hmf}}{\rho_f} \frac{\text{Re}}{Fr} \cos \lambda \end{aligned} \quad (20)$$

$$\text{Pr Re} \left(\frac{(\rho C_p)_{hmf}}{(\rho C_p)_f} \right) \left(\frac{k_f}{k_{hmf}} \right) \left[\frac{\partial \theta}{\partial t} + \delta \varepsilon u \frac{\partial \theta}{\partial r} + \varepsilon w \frac{\partial \theta}{\partial z} \right] = \left[\frac{\partial^2 \theta}{\partial r^2} + \frac{1}{r} \frac{\partial \theta}{\partial r} + \varepsilon^2 \frac{\partial^2 \theta}{\partial z^2} \right] + \left(\frac{k_f}{k_{hmf}} \right) \beta \quad (21)$$

Additionally, the non-dimensional form of the geometry represented by Eqn. (1) is given as:

$$R(z) = \left\{ \begin{aligned} & \left[(m_1 z + 1) - \frac{\delta_i}{2} \left\{ 1 + \cos 2\pi \left(z - \alpha_i - \frac{1}{2} \right) \right\} \right], & \alpha_i \leq z \leq \alpha_i + 1, \\ & (m_1 z + 1), & \text{otherwise} \end{aligned} \right. \quad (22)$$

Subsequently, with the help of Burton [42], the *axial pressure gradient* can be represented as:

$$-\left(\frac{\partial p}{\partial z} \right) = A_0 + A_1 \cos(2\pi \omega_p t), \quad t > 0 \quad (23)$$

It is noteworthy that A_0 is the mean pressure gradient and A_1 denotes the amplitude of the pulsatile component, which is subjected to diastolic and systolic pressures. By using non-dimensionalized parameters, the normalized form of Eqn. (23) becomes:

$$-\left(\frac{\partial p}{\partial z} \right) = B_1 (1 + e \cos(c_1 t)) \quad (24)$$

$$\text{Here } e = \frac{A_1}{A_0}, B_1 = \frac{A_0 R_0^2}{U_0 \mu_o}, \omega_p = 2\pi f_p, c_1 = \frac{R_0 \omega_p}{U_0} \quad (25)$$

The equations for the thermophysical parameters of a *unitary nanofluid* are represented following [41] by the relations:

$$\begin{aligned} \mu_{nf}(\theta) &= \frac{\mu_f}{(1-\phi)^{5/2}}, & \rho_{nf} &= (1-\phi)\rho_f + \phi\rho_s \\ (\rho C_p)_{nf} &= (1-\phi)(\rho C_p)_f + \phi(\rho C_p)_s, & (\rho\gamma)_{nf} &= (1-\phi)(\rho\gamma)_f + \phi(\rho\gamma)_s \\ \frac{k_{nf}}{k_f} &= \frac{k_s + (n_2 - 1)k_f - (n_2 - 1)\phi(k_f - k_s)}{k_s + (n_2 - 1)k_f + \phi(k_f - k_s)} \end{aligned} \quad (26)$$

Additionally, the equations for thermo-physical properties of *hybrid mediated nanofluid* are presented as [41]:

$$\begin{aligned} \mu_{hmf} &= \frac{\mu_f}{(1-\phi_1)^{5/2}(1-\phi_2)^{5/2}}, & \rho_{hmf} &= (1-\phi_2)[(1-\phi_1)\rho_f + \phi_1\rho_{s_1}] + \phi_2\rho_{s_2} \\ (\rho C_p)_{hmf} &= (1-\phi_2)[(1-\phi_1)(\rho C_p)_f + \phi_1(\rho C_p)_{s_1}] + \phi_2(\rho C_p)_{s_2} \\ (\rho\gamma)_{hmf} &= (1-\phi_2)[(1-\phi_1)(\rho\gamma)_f + \phi_1(\rho\gamma)_{s_1}] + \phi_2(\rho\gamma)_{s_2} \\ \frac{k_{hmf}}{k_{bf}} &= \frac{k_{s_2} + (n_2 - 1)k_{bf} - (n_2 - 1)\phi_2(k_{bf} - k_{s_2})}{k_{s_2} + (n_2 - 1)k_{bf} + \phi_2(k_{bf} - k_{s_2})}, \text{ where } \frac{k_{bf}}{k_f} = \frac{k_{s_1} + (n_2 - 1)k_f - (n_2 - 1)\phi_1(k_f - k_{s_1})}{k_{s_1} + (n_2 - 1)k_f + \phi_1(k_f - k_{s_1})} \end{aligned} \quad (27)$$

In the above-mentioned equations, μ_f is the viscosity, ρ_f is density, $(\rho C_p)_f$ is heat capacitance, γ_f is thermal expansion coefficient and k_f is the thermal conductivity of the *base fluid*. For different nanoparticles, (ϕ_1, ϕ_2) represent volume fractions, (ρ_{s_1}, ρ_{s_2}) are the densities of solid nanoparticles, $[(\rho C_p)_{s_1}, (\rho C_p)_{s_2}]$ are the heat capacitances, $[\gamma_{s_1}, \gamma_{s_2}]$ are thermal expansion coefficients and $[k_{s_1}, k_{s_2}]$ designate the thermal conductivities of solid nanoparticles, respectively. Here n_2 is the shape factor of the nanoparticles. Various nanoparticle shapes with corresponding shape factors are given in **Table 1**.




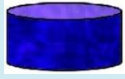

Shape of Nanoparticles	Shape Image	Shape factor (n ₂)	Corresponding Hybrid Thermal Conductivity
Circle		3.0	$\frac{k_{hnf}}{k_{bf}} = \frac{k_{S_2} + 2k_{bf} - 2\phi_2(k_{bf} - k_{S_2})}{k_{S_2} + 2k_{bf} + \phi_2(k_{bf} - k_{S_2})}$
Bricks		3.7	$\frac{k_{hnf}}{k_{bf}} = \frac{k_{S_2} + 2.7k_{bf} - 2.7\phi_2(k_{bf} - k_{S_2})}{k_{S_2} + 2.7k_{bf} + \phi_2(k_{bf} - k_{S_2})}$
Cylinders		4.9	$\frac{k_{hnf}}{k_{bf}} = \frac{k_{S_2} + 3.9k_{bf} - 3.9\phi_2(k_{bf} - k_{S_2})}{k_{S_2} + 3.9k_{bf} + \phi_2(k_{bf} - k_{S_2})}$
Platelets		5.7	$\frac{k_{hnf}}{k_{bf}} = \frac{k_{S_2} + 4.7k_{bf} - 4.7\phi_2(k_{bf} - k_{S_2})}{k_{S_2} + 4.7k_{bf} + \phi_2(k_{bf} - k_{S_2})}$
Blades		8.6	$\frac{k_{hnf}}{k_{bf}} = \frac{k_{S_2} + 7.6k_{bf} - 7.6\phi_2(k_{bf} - k_{S_2})}{k_{S_2} + 7.6k_{bf} + \phi_2(k_{bf} - k_{S_2})}$

Table 1: Various nanoparticle shapes with associated shape factors

In reference to further analysis, two different hypotheses have been taken into account; $\delta \ll 1$ and $\varepsilon = O(1)$ i.e. *stenosis height parameter is greatly less than unity*, and the *vessel aspect ratio is of comparable magnitude to unity*. After imposing these suppositions, Eqns. (18)-(21) will be reduced to a system of coupled differential equations. Further, for restraining the geometric effects, the radial coordinate transformation $x = \frac{r}{R(z)}$ is employed in the reduced governing equations. Hence

applying the transformation and after putting the non-dimensionalized form of pressure gradient, Eqns. (18)-(21) are changed into the following form:

$$\left(\frac{\rho_{hnf}}{\rho_f}\right) \text{Re} \left[\frac{\partial w}{\partial t} \right] = B_1 (1 + e \cos(c_1 t)) + \left[\frac{1}{xR^2} \frac{\partial}{\partial x} \left(x \left\{ m + (1+m) \left(1 + \left(\frac{\gamma}{R} \right)^2 \left| \left(\frac{\partial w}{\partial x} \right)^2 \right|^{\frac{n-1}{2}} \right\} \left(\frac{\partial w}{\partial x} \right) \right) \right] + \frac{(\rho\gamma)_{hnf}}{(\rho\gamma)_f} Gr \theta \sin \lambda + \frac{\rho_{hnf}}{\rho_f} \frac{\text{Re}}{Fr} \sin \lambda \quad (28)$$

$$\text{Pr Re} \left(\frac{(\rho C_p)_{hmf}}{(\rho C_p)_f} \right) \left(\frac{k_f}{k_{hmf}} \right) \left[\frac{\partial \theta}{\partial t} \right] = \frac{1}{R^2} \left[\frac{\partial^2 \theta}{\partial x^2} + \frac{1}{x} \frac{\partial \theta}{\partial x} \right] + \left(\frac{k_f}{k_{hmf}} \right) \beta \quad (29)$$

Further, Eqns. (13)-(15) are prescribed the following boundary and initial conditions:

$$w(x,t)|_{x=1} = w_B, \quad \theta(x,t)|_{x=1} = 1, \quad w(x,t)|_{x=R_c} = 0, \quad \theta(x,t)|_{x=R_c} = 0 \quad (30)$$

$$w(x,0) = 0, \quad \theta(x,0) = 0 \quad (31)$$

$$\frac{\partial w}{\partial x} = \frac{\alpha}{\sqrt{Da}} [w_B - w_{porous}] \quad (32)$$

Similarly, the volumetric flow rate and wall shear stress (WSS) respectively are presented by the following form:

$$Q_1 = 2\pi R^2 \left(\int_0^1 w x dx \right), \quad (33)$$

$$\tau_s = -\frac{1}{R} \left(\frac{\partial w}{\partial x} \right)_{x=1}, \quad (34)$$

5. Numerical solution with FTCS scheme:

In this scheme, firstly the spatial domain is discretized and after that, the value of velocity component is calculated at each node x_i and over the time instant t^k , which is written as w_i^k . According to Hoffmann [43], the central differencing formulation for second order and forward differencing formulation for first order partial derivatives are defined respectively as:

$$\frac{\partial w}{\partial x} \cong \frac{w_{i+1}^k - w_{i-1}^k}{2\Delta x} = w_x \quad (35)$$

$$\frac{\partial^2 w}{\partial x^2} \cong \frac{w_{i+1}^k - 2w_i^k + w_{i-1}^k}{(\Delta x)^2} = w_{xx} \quad (36)$$

and

$$\frac{\partial w}{\partial t} \cong \frac{w_i^{k+1} - w_i^k}{(\Delta t)} \quad (37)$$

Incorporating the values of described partial derivatives, Eqns. (28)-(29) will take the following form:

$$w_i^{k+1} = w_i^k + \frac{\Delta t}{\text{Re} \left[(1-\phi_2) \left[(1-\phi_1) + \phi_1 \frac{\rho_{S_1}}{\rho_f} \right] + \phi_2 \frac{\rho_{S_2}}{\rho_f} \right]} \left[\begin{aligned} & B_1 [1 + e \cos(c_1 t^k)] + \left[\frac{1}{xR^2} \frac{\partial}{\partial x} \left[x \left\{ m + (1+m) \left(1 + \frac{\gamma^2}{R^2} \left(\left| \frac{\partial w}{\partial x} \right| \right)^2 \right)^{\frac{n-1}{2}} \right\} \left(\frac{\partial w}{\partial x} \right) \right] \right] \\ & + \left[(1-\phi_2) \left[(1-\phi_1) + \phi_1 \frac{(\rho\gamma)_{S_1}}{(\rho\gamma)_f} \right] + \phi_2 \frac{(\rho\gamma)_{S_2}}{(\rho\gamma)_f} \right] Gr \sin \lambda \theta_i^k + \\ & \left[(1-\phi_2) \left[(1-\phi_1) + \phi_1 \frac{\rho_{S_1}}{\rho_f} \right] + \phi_2 \frac{\rho_{S_2}}{\rho_f} \right] \left(\frac{\text{Re}}{\text{Fr}} \right) \sin \lambda \end{aligned} \right] \quad (38)$$

$$\theta_i^{k+1} = \theta_i^k + \left(\frac{k_{hmf}}{k_f} \right) \frac{\Delta t}{\text{Pr Re} \left[(1-\phi_2) \left[(1-\phi_1) + \phi_1 \frac{(\rho C_p)_{S_1}}{(\rho C_p)_f} \right] + \phi_2 \frac{(\rho C_p)_{S_2}}{(\rho C_p)_f} \right]} \left\{ \left(\frac{1}{R^2} \right) \left[\frac{\partial^2 \theta}{\partial x^2} + \frac{1}{x} \frac{\partial \theta}{\partial x} \right] + \frac{k_f}{k_{hmf}} \beta \right\} \quad (39)$$

Further, the associated boundary and initial conditions for Eqns. (38)-(39) emerge as:

$$w_i^1 = \theta_i^1 = 0, \quad \text{at } t = 0 \quad (40)$$

$$w_{N+1}^k = w_B, \quad \theta_{N+1}^k = 1, \quad \text{at } x = 1, \quad w_1^k = \theta_1^k = 0, \quad \text{at } x = R_c \quad (41)$$

$$\frac{\partial w}{\partial x} = \frac{\alpha}{\sqrt{Da}} [w_B - w_{porous}] \quad (42)$$

In the FTCS numerical scheme, the spatial variable is discretized into $N+1$ grid-points, where step size is taken as $\Delta x = \frac{1}{N+1}$. The time instant is defined by t_k , where the value of t_k is given as $t_k = (k-1)\Delta t$, in which Δt shows the small increment in time. The velocity component is further calculated at each node and for every time instant. As stability of this numerical scheme is dependent on both step size and time increment, hence $\Delta x = 0.025$ and $\Delta t = 0.0001$ are selected to fulfill the stability condition.

6. Validation of FTCS numerical scheme:

Validation of the applied FTCS numerical scheme is done by comparing solutions for the current problem with the numerical results obtained by Ijaz and Nadeem [44]. The *axial blood velocity for different nanoparticle concentrations* was compared for the present computations. The validation is documented in **Table 2** both for normal blood i.e. without nanoparticles ($\phi=0.00$) and for blood doped with nanoparticles ($\phi=0.02$) at the *throat of the stenotic artery* ($z=1.5$) and $t=1.2$. In both cases, *first flow acceleration and then deceleration was observed* with increasing radial coordinate (r). Evidently very close correlation is achieved and confidence in the present FTCS scheme is therefore justifiably high.

Radius	Ijaz and Nadeem [44] $\phi=0.00, \delta=0.01$	Present FTCS results	Ijaz and Nadeem [44] $\phi=0.02, \delta=0.01$	Present FTCS results
0.1	0.00	0.00	0.000	0.000
0.2	0.0317	0.0319	0.0645	0.0649
0.3	0.0418	0.0422	0.0820	0.0826
0.4	0.0420	0.0425	0.0776	0.0782
0.5	0.0366	0.0369	0.0613	0.0618
0.6	0.0283	0.0288	0.0390	0.0394
0.7	0.0191	0.0199	0.0152	0.0181
0.8	0.0109	0.0110	-0.0060	0.0064
0.9	0.0052	0.0055	-0.0206	-0.0210
1.0	0.0039	0.0039	-0.0248	-0.0248

Table 2: Comparison of FTCS code results with Ijaz and Nadeem [44] for axial velocity at throat of stenotic artery $z=1.5$ and $t=1.2$

7. Numerical results and discussion:

In this section, the hemodynamic characteristics in the artery having mild stenosis and aneurysm in the presence of hybrid nanoparticles are computed. Considering the emerging parameters, the results for the thermophysical properties such as *axial flow velocity, temperature, wall shear stress and volumetric flow rate* are visualized graphically in **Figures 2- 35**. The figures show the

comparison for the hemodynamic characteristics *at the stenosis and aneurysm regions* and for *three different arterial tapering scenarios* (non-tapered, diverging, converging). **Table 3** presents the default values for the key parameters implemented in the FTCS computations while **Table 4** presents the considered range of parameters in the computations.

Φ_1	Φ_2	W_b	Re	Pr	Fr	m	n	β	λ	\sqrt{Da}	Gr	B_1	α
0.03	0.03	0.1	2	14	0.9	0.175	0.7	0.2	60°	0.1	2	1.41	0.1

Table 3: Default values of emerging parameters

Parameter	ϕ_1, ϕ_2	w_b	Fr	β	α	Pr	Re	Gr	m	\sqrt{Da}	B_1
Range	0.01-0.05	0.0-0.2	0.1-0.9	0.1-1.0	0.05-0.2	7-21	1-5	1-5	0.175-0.775	0.05-0.2	1.41-6.6

Table 4: Considered range of emerging parameters

Figures 2 (a)-(b) represents the influence of unitary (silver) nanoparticle volume fraction (ϕ_1) (range 0.00-0.05) on blood flow velocities at the stenosis and aneurysm regions, respectively. These graphs are also visualized for different tapering behaviour of the artery. The graphs show that with increasing nanoparticle volume fraction (ϕ_1), acceleration is computed in both regions. The results are also supported by Ahmed and Nadeem [22] study, which was conducted for the blood flow through curved artery with catheterized stenosis. Higher magnitudes of velocity are attained for the *diverging* tapered artery comparing to the *non-tapered* and *converging* artery cases. It is also evident that axial velocity is greater at the aneurysm region for various volume fractions compared with the stenotic region. In all plots, the velocity is maximum at the centerline of the artery and decreases to the vessel wall at which it attains the value of the slip velocity (w_B).

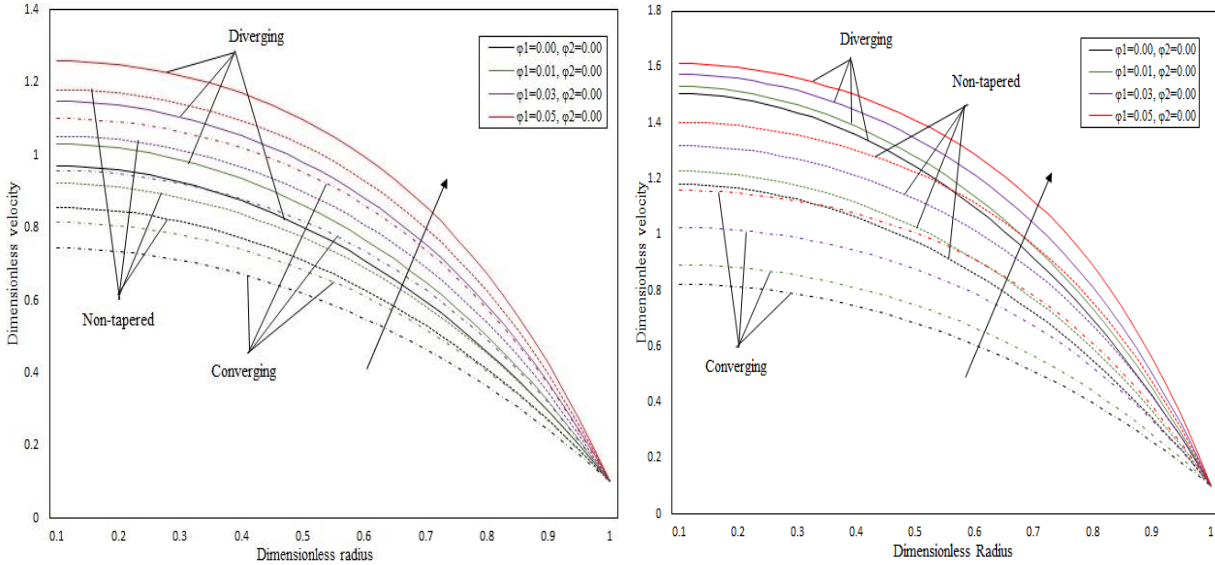


Figure 2: Effect of nanoparticle concentration on axial velocity with *Ag nanofluid only* at (a) stenosis (b) aneurysm and $B_1 = 1.41, \delta = 0.1, t = 1.2$.

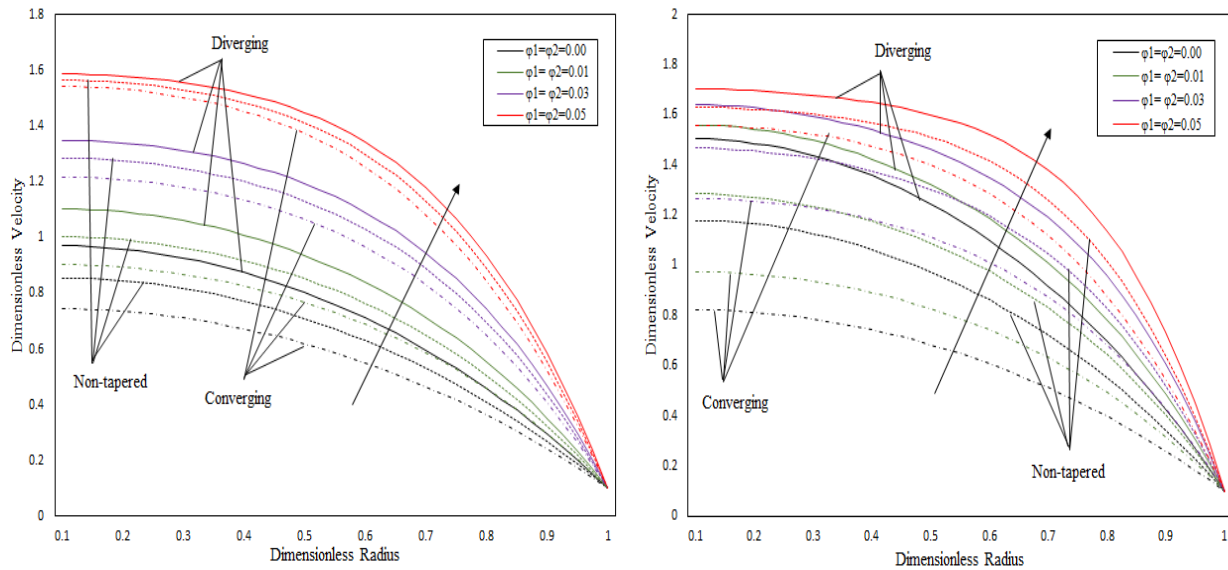


Figure 3: Effect of nanoparticle concentration on axial velocity with (*Ag+Cu*) hybrid nanofluid at (a) stenosis (b) aneurysm and $B_1 = 1.41, \delta = 0.1, t = 1.2$.

Similarly, **Figures 3 (a)-(b)** shows the effect of hybrid nanoparticle concentration ($\phi_1+\phi_2$) (range 0.00-0.05) on axial velocity profile at the stenosis and aneurysm locations. As volume fraction is increased, there is a significant enhancement in velocity profile in both figures. Axial flow is therefore accelerated considerably with higher volume fractions of silver and copper nanoparticles. These two figures also follow the same behaviour for the tapering effect as computed earlier in Figure 2. On comparing both figures of Figure 3 with Figure 2, it is found that addition of a second

nanoparticle type exacerbates the increment in velocity value and this result is extremely favorable since hemodynamic acceleration is desirable for mitigating arterial diseases [3, 6].

Figures 4 (a)-(b) visualize the temperature profile response across the artery cross section (i.e. with radial coordinate) to different volume concentration of silver nanoparticles (ϕ_1) again at the stenosis and aneurysm regions, respectively. Evidently as the volume fraction is increased, there is a marked increment in temperature magnitudes for both zones at the throat of the stenotic artery. Thermal enhancement is therefore achieved with greater doping of silver nanoparticles and this is due to the elevation in thermal conductivity of blood with nanoparticle presence. Contrary to the velocity profiles, however, it is seen that higher temperature magnitudes are acquired for the *converging artery* compared to the non-tapered and diverging artery. Similarly, **Figures 5 (a)-(b)** depict the temperature variation for various concentrations of hybrid nanoparticles ($\phi_1+\phi_2$). As volume fraction is increased from 0.00 (absence of nanoparticles i.e. pure blood) to 0.05, temperature is also found to be increased in the same manner. Comparing Figure 5 with Figure 4 it may be noted that greater increases are registered for the *hybrid nanofluid* (silver and copper nanoparticles) case than for the *unitary nanofluid* (only silver nanoparticles). Again, this is due to the boost in thermal conductivity achieved with both silver and copper, relative to just silver nanoparticles alone. Also, a slight difference is observed in the temperature profiles between the stenosis (constriction) and aneurysm (bulge) region and temperature is consistently greater in the stenotic region.

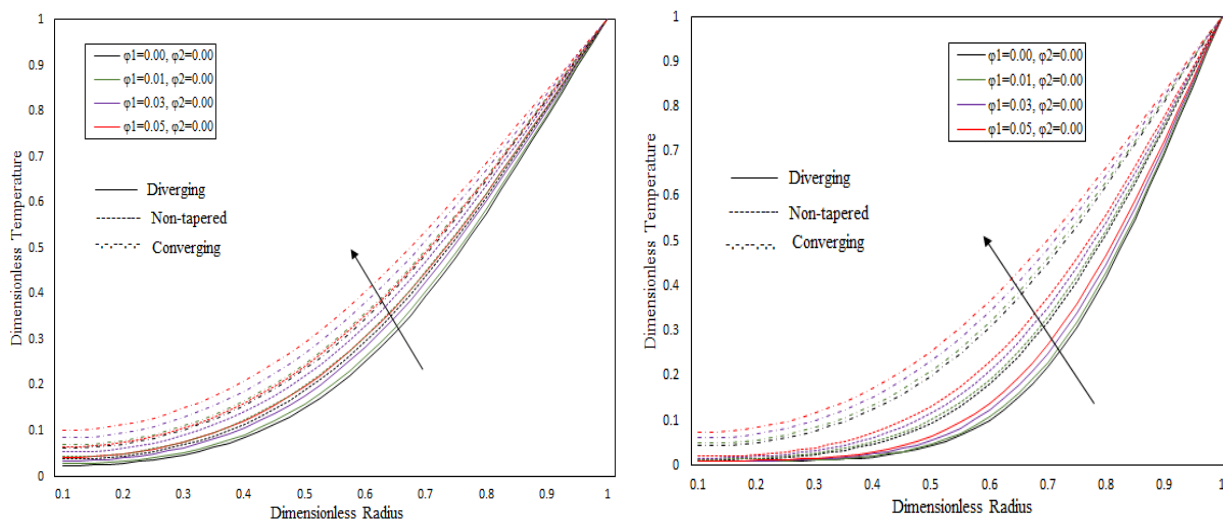


Figure 4: Effect of nanoparticle concentration on temperature profile with *Ag nanofluid only* at (a) stenosis (b) aneurysm and $B_1 = 1.41$, $\delta = 0.1$, $t = 1.2$.

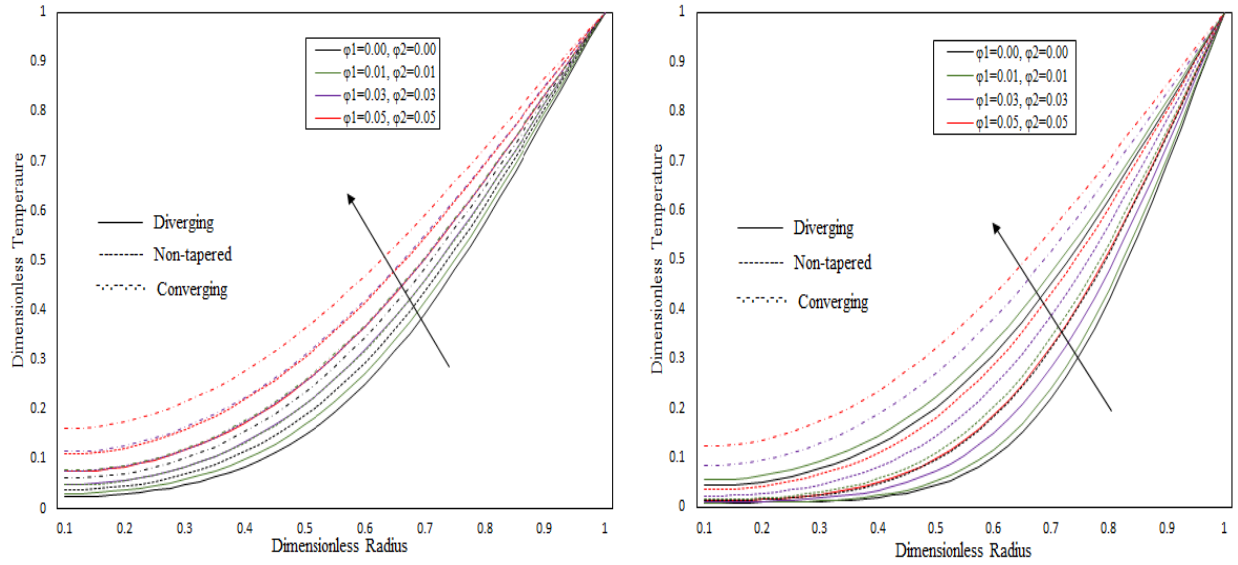


Figure 5: Effect of nanoparticle concentration on temperature profile with $(Ag+Cu)$ hybrid nanofluid at (a) stenosis (b) aneurysm and $B_1 = 1.41, \delta = 0.1, t = 1.2$.

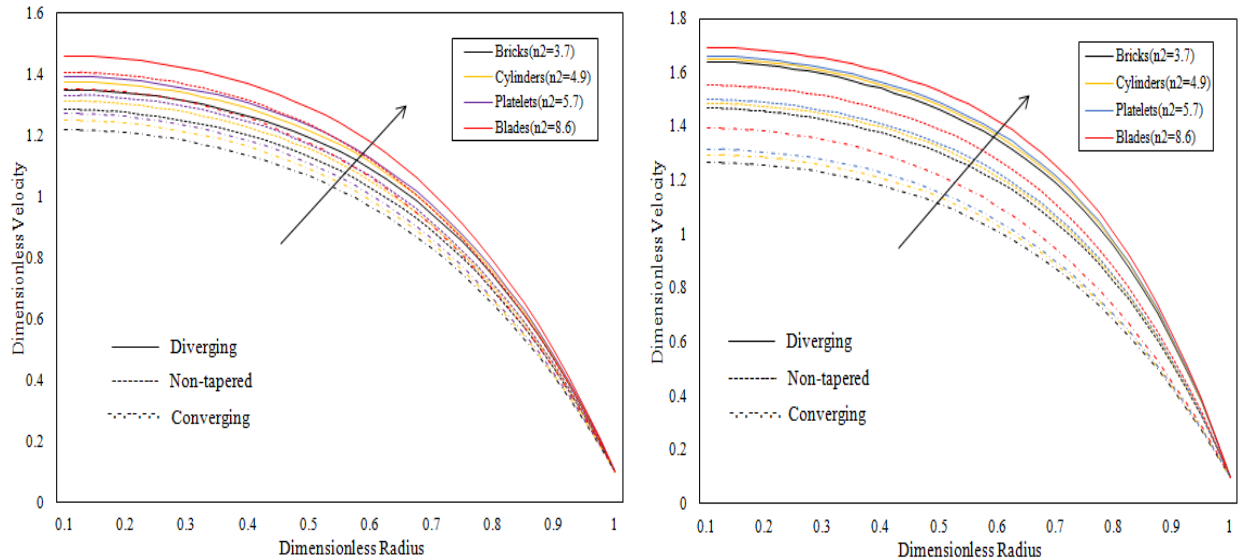


Figure 6: Effect of shape parameter (n_2) on axial velocity with $(Ag+Cu)$ hybrid nanofluid at (a) stenosis (b) aneurysm and $B_1 = 1.41, \delta = 0.1, t = 1.2$.

Figures (6)-(7) illustrate the impact of different values of shape parameter of nanoparticles on velocity and temperature profiles, respectively. **Figure 6 (a)-(b)** exhibits the axial velocity distribution at the stenosis and aneurysm region for the tapered (diverging or converging) and non-tapered artery cases. The graphs indicate that on changing the shape of nanoparticles from the bricks, then cylinders, then platelets to finally blades i.e. increasing the shape parameter (n_2) from 3.7 to 4.9 to 5.7 and eventually to 8.6, there is an apparent enhancement in velocity profile at the

throat of the stenotic artery and also in the aneurysmal region. Increasing the shape parameter results in an elevation in thermal conductivity of the hybrid nanofluid (since greater surface area encourages micro-convection in the vicinity of the nanoparticles) and this manifests in an accentuation in thermal diffusion in the hybrid nanofluid. This accelerates the *axial flow*. Results for the acceleration of velocity profile are supported by Ijaz and Nadeem [52] study, which elaborates the influence of hybrid nanoparticles on hemodynamics through overlapped stenotic artery. Higher magnitudes of velocity are computed for the *diverging artery* case, *both at the stenosis and also the aneurysm*, although velocity at the aneurysm is always slightly higher than at the stenosis. Similarly, **figure 7 (a)-(b)** shows the changes in temperature profile with an increment in the shape of nanoparticles at the stenosis and aneurysm. Temperature is strongly boosted on increasing the shape parameter from 3.7 to 8.6 i.e. *brick nanoparticles* produce minimal temperatures whereas *blade-shaped nanoparticles* achieve maximum temperatures. Furthermore, a higher amplitude is noticed for the converging artery case relative to the diverging and non-tapered cases and this is exactly the opposite behaviour to that computed for the velocity profile.

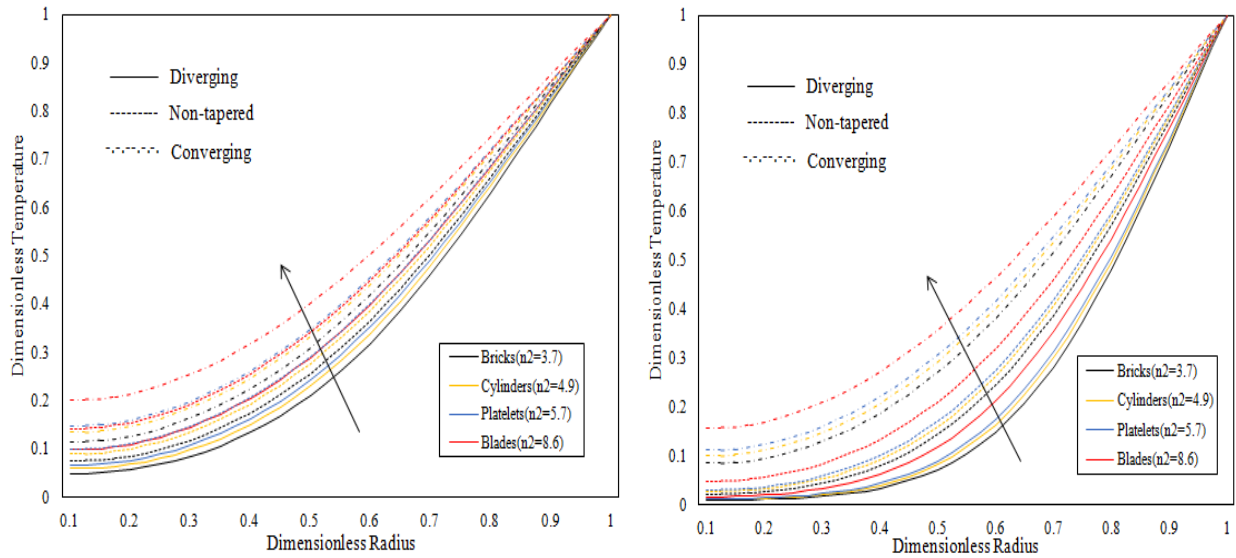


Figure 7: Effect of shape parameter (n_2) on temperature profile with $(Ag+Cu)$ hybrid nanofluid at (a) stenosis (b) aneurysm and $B_1 = 1.41, \delta = 0.1, t = 1.2$.

Figures 8 and 9 visualize the evolution in axial velocity profiles for different Froude number (Fr) (range 0.1-0.9) and slip velocity (w_B) for $(Ag+Cu)$ hybrid nanofluid. **Figure 8 (a)-(b)** show that on increasing the Froude number from 0.1 to 0.9, there is a remarkable decrement in the velocity value in both stenosis and aneurysm. Froude number embodies the relative contribution of inertial

force to gravity force in the hemodynamic regime. It features however in the denominator of the supplementary body force term, $+\frac{\rho_{hnf} Re}{\rho_f Fr \sin \lambda}$ in the axial momentum conservation Eqn. (40). Higher values of Fr (*with all other parameters fixed*) therefore reduce the contribution of this body force to the blood flow and this manifests in a deceleration, as observed in Figs 8a,b. Diverging arteries attain higher values of axial velocity in comparison with non-tapered and converging arteries; momentum transport is assisted with the *diverging geometry* whereas it is inhibited with converging geometries or even the conventional non-tapered case by virtue of the continuity principle for incompressible flow.

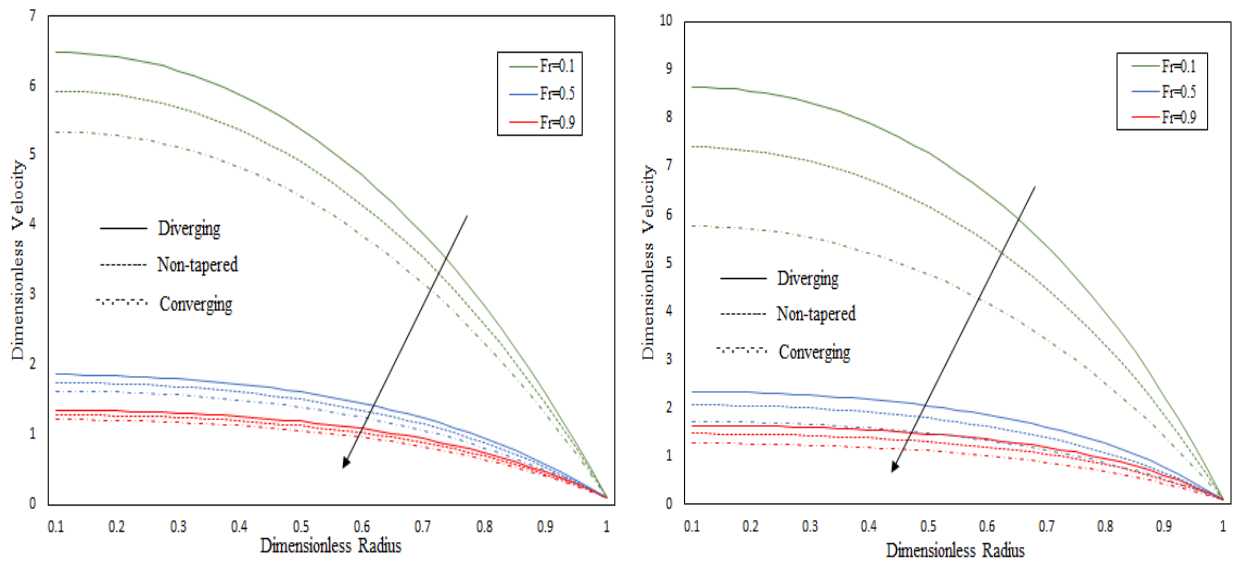


Figure 8: Effect of Froude number (Fr) on axial velocity with $(Ag+Cu)$ hybrid nanofluid at (a) stenosis (b) aneurysm and $B_1 = 1.41$, $\delta = 0.1$, $t = 1.2$.

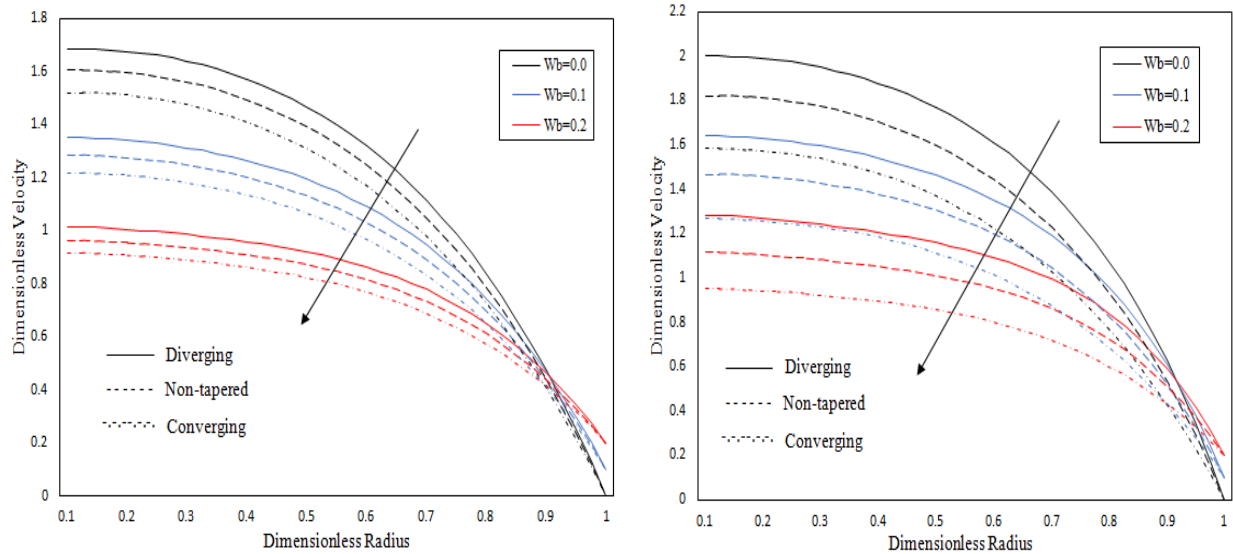


Figure 9: Effect of Slip velocity (W_b) on axial velocity with $(Ag+Cu)$ hybrid nanofluid at (a) stenosis (b) aneurysm and $B_1 = 1.41, \delta = 0.1, t = 1.2$.

In **figure 9 (a)-(b)**, with increasing *wall slip* parameter (range 0.0-0.2), *deceleration* in axial velocity is noticed. The slip parameter is a boundary condition which is imposed at the inner surface of the arterial wall. The presence of the slip velocity induces a momentum retardation and velocity delay which impedes the blood in the near-wall regime and decelerates the axial blood flow, although the effect clearly decays with further radial distance toward the arterial center line. In the aneurysm region, velocity is always higher than at the stenotic region and diverging arteries *produce a maximum value* in comparison to converging and non-tapered arteries.

Figures 10-11 illustrate the effect of heat generation parameter (β) (range 0.1-1.0) on velocity and temperature profiles for hybrid nanofluid. This effect may correspond for example to spot thermal therapy in laser treatment in medicine. An increase in this parameter from 0.1 to 1.0 shows a noticeable impact on temperature profile (Fig. 11) whereas it produces a much more prominent enhancement in velocity (Fig. 10), in particular, near the centerline of the arterial zone. Ijaz and Nadeem [44] also showed the same influence of heat generation parameter on velocity profile through catheterized composite stenosed artery. Towards the vessel periphery there is a progressive diminishing in the influence of heat generation and all profiles merge. Marked differences can be seen with the *tapering effect* on both velocity and temperature profiles. Diverging arteries attain the maximum velocity magnitudes whereas converging arteries achieve the maximum temperatures. For axial velocity, magnitudes are always highest in the aneurysm

region compared to the stenosis region; however, a smaller difference is seen in the case of temperature.

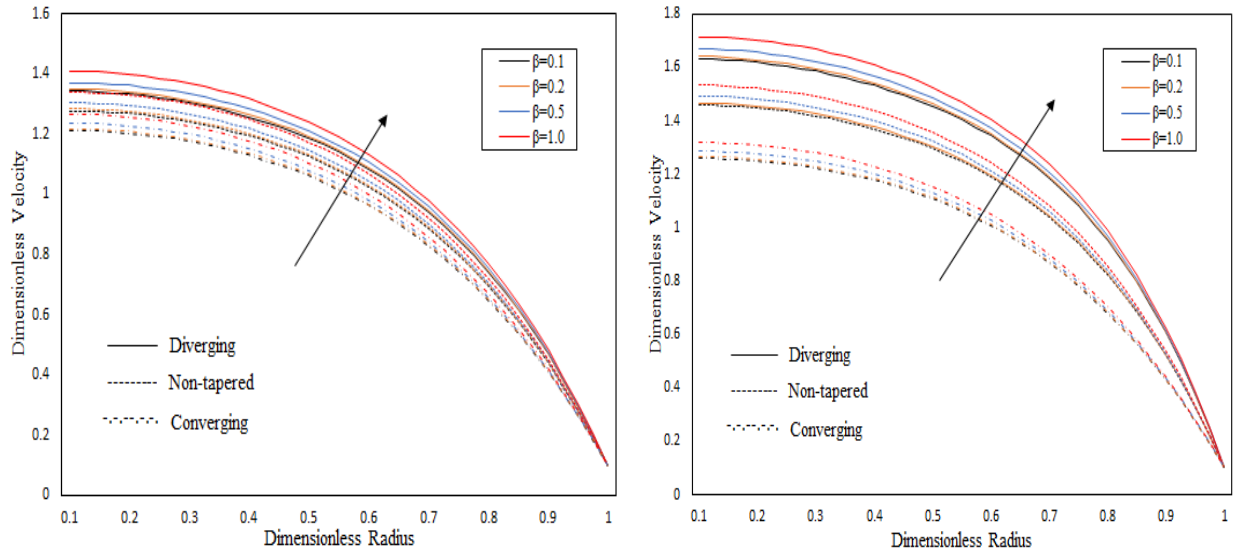


Figure 10: Effect of heat generation parameter (β) on axial velocity with $(Ag+Cu)$ hybrid nanofluid at (a) stenosis (b) aneurysm and $B_1 = 1.41$, $\delta = 0.1$, $t = 1.2$.

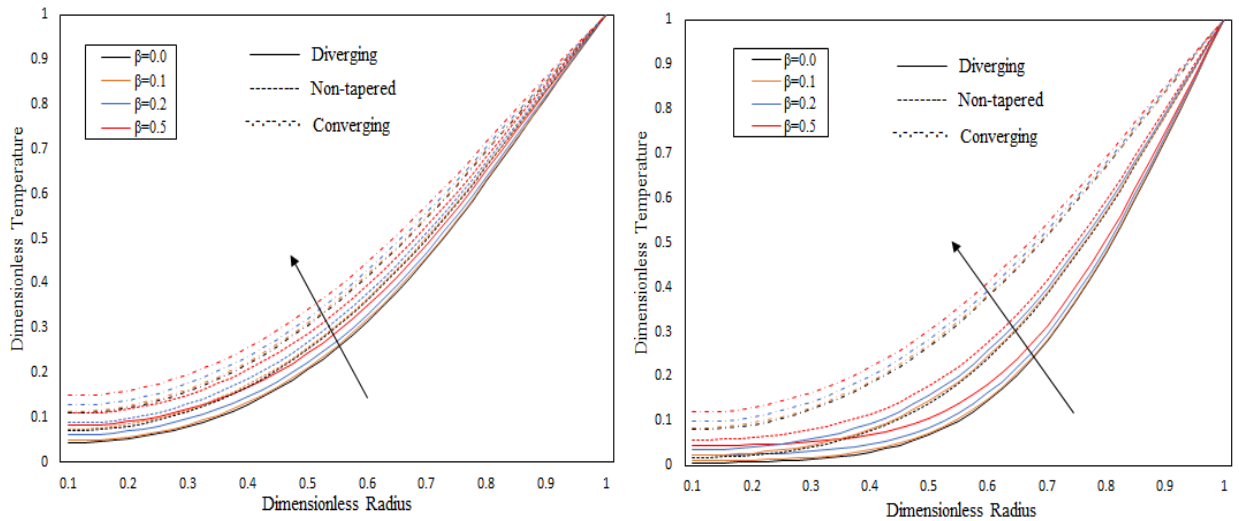


Figure 11: Effect of heat generation parameter (β) on temperature profile with $(Ag+Cu)$ hybrid nanofluid at (a) stenosis (b) aneurysm and $B_1 = 1.41$, $\delta = 0.1$, $t = 1.2$.

Figure 12 (a)-(b) depicts the influence of porous parameter (α) (range 0.05-0.2) on axial velocity profiles at the stenosis and aneurysm regions, respectively. In both cases, when we increase the porous parameter from 0.05 to 0.2, then removal of blood via the permeable arterial wall is increased- this inhibits momentum diffusion in the axial flow and results in axial flow retardation.

The porous parameter features only in the arterial wall boundary condition i.e.

$$\frac{\partial w}{\partial x} = \frac{\alpha}{\sqrt{Da}} [w_B - w_{porous}] \text{ in Eqn. (44). The same favorable result is produced by Ijaz and Nadeem}$$

[44] for the impact of porous parameter (α) on flow velocity by considering the permeability effect on arterial wall. Evidently, the diverging tapered artery produces a higher axial velocity in comparison with the non-tapered and converging artery cases.

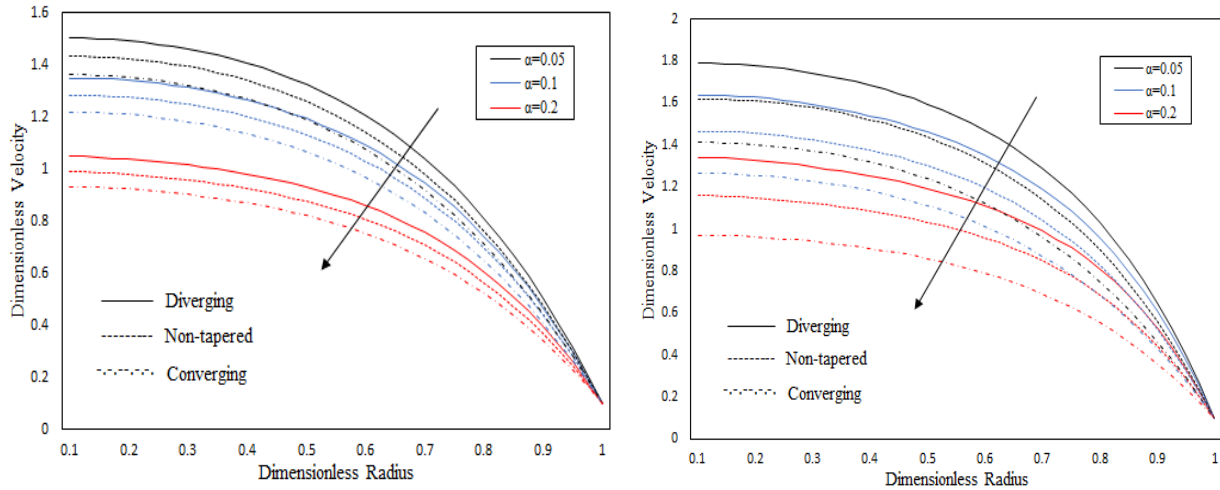


Figure 12: Effect of porous parameter (α) on axial velocity with $(Ag+Cu)$ hybrid nanofluid at (a) stenosis (b) aneurysm and $B_1 = 1.41, \delta = 0.1, t = 1.2$.

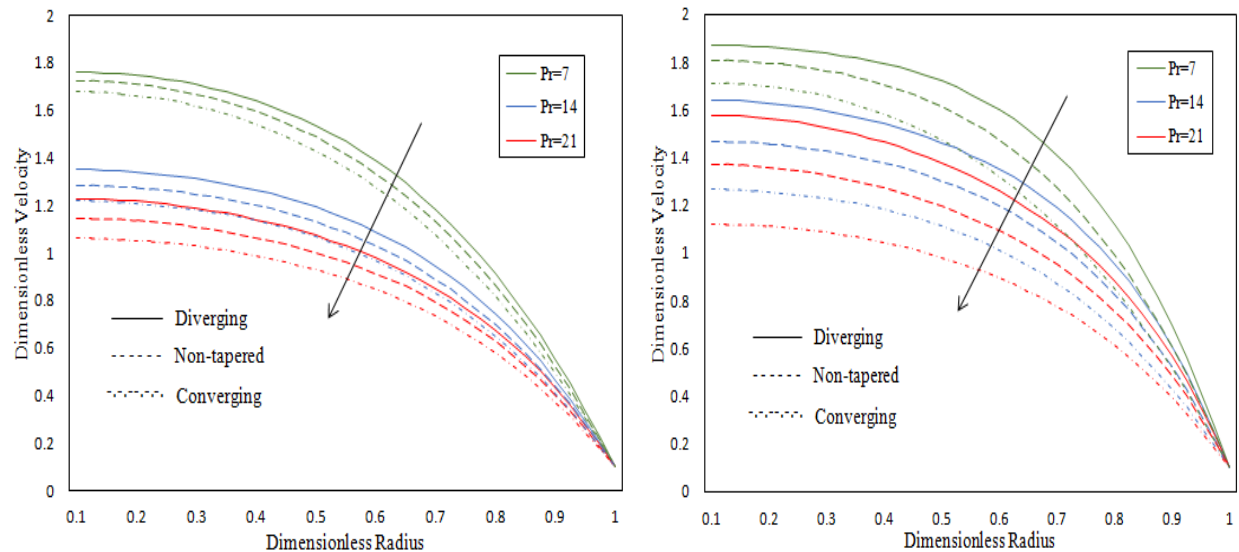


Figure 13: Effect of Prandtl number (Pr) on axial velocity with $(Ag+Cu)$ hybrid nanofluid at (a) stenosis (b) aneurysm and $B_1 = 1.41, \delta = 0.1, t = 1.2$.

Figure 13 (a)-(b) and 14 (a)-(b) shows the velocity and temperature profile for various Prandtl numbers (Pr) (range 7-21) again at both stenosis and aneurysm regions. It is demonstrated that flow deceleration and cooling are produced with an increase in value of Pr from 7 to 21 at the throat of the artery. Prandtl number is the ratio of momentum diffusivity to thermal diffusivity, which implies that Pr is inversely related to heat transfer from the artery wall to the fluid. When Pr is significantly small ($Pr < 1$), the momentum diffusion rate is much lower than thermal diffusion rate. The curve trends in Figure 13 and 14 confirm that with higher Prandtl number, velocity plummets as does temperature magnitude (this will correspond to thicker momentum boundary layer at the arterial wall and a thinner thermal boundary layer). Mitvalsky [45] has emphasized that in the normal room temperature range, 19 - 30.8 Celsius, laminar streaming blood has a Prandtl number between 15 and 25. Of course these values are reduced with the doping of metallic nanoparticles and therefore the range studied in the present simulations i.e. Pr of 7 to 21 is appropriate for hemodynamics. Blood therefore has a much higher momentum diffusivity comparing to thermal diffusivity. Diller [46] and Hensley *et al.* [47] elaborated that this property is necessary for thermoregulation and other biothermal functions. It is also noted that for the velocity distribution, the *aneurysm region* exhibits the peak value whereas for the temperature profiles, the *stenotic zone* produces the highest values.

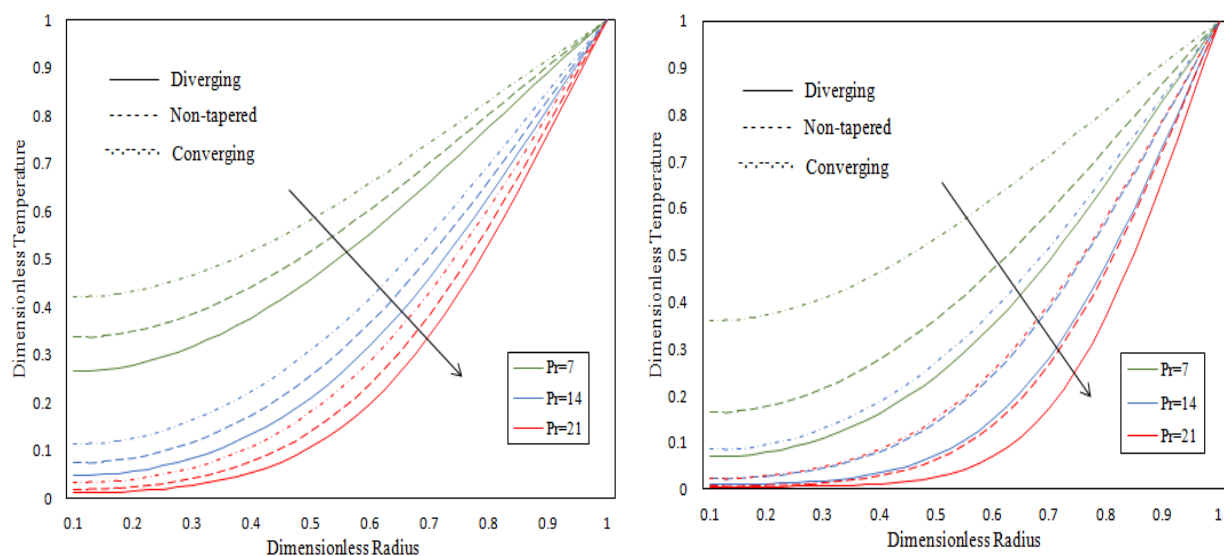


Figure 14: Effect of Prandtl number (Pr) on temperature profile with $(Ag+Cu)$ hybrid nanofluid at (a) stenosis (b) aneurysm and $B_1 = 1.41, \delta = 0.1, t = 1.2$.

The effect of Reynolds number (Re) (range 1-5) on blood flow velocity and temperature profile is displayed in **Figure 15 (a)-(b)** and **16 (a)-(b)**. It is noteworthy that very low Reynolds numbers are considered laminar flow and the regime is therefore a *viscous dominated* one. On increasing the value of Re from 1 to 5, a significant amount of reduction in velocity has been seen. In the same manner, as we increased the magnitude of Re , the magnitude of temperature is also decreased. Although inertial force is increased with Reynolds number, the overwhelming effect is nevertheless flow deceleration owing to the stenotic obstruction and presence of nanoparticles. Substantial deviation in values is computed in the stenosis and aneurysm regions. As in velocity case, the magnitude is higher for all Reynolds number in aneurysm region while for temperature case, the reverse trend is observed (values are higher in the stenosis region). For the velocity profile, the *diverging artery case* produces a higher value compared to the non-tapered and converging arteries. Conversely, the *converging artery case* attains the maximum temperature magnitude.

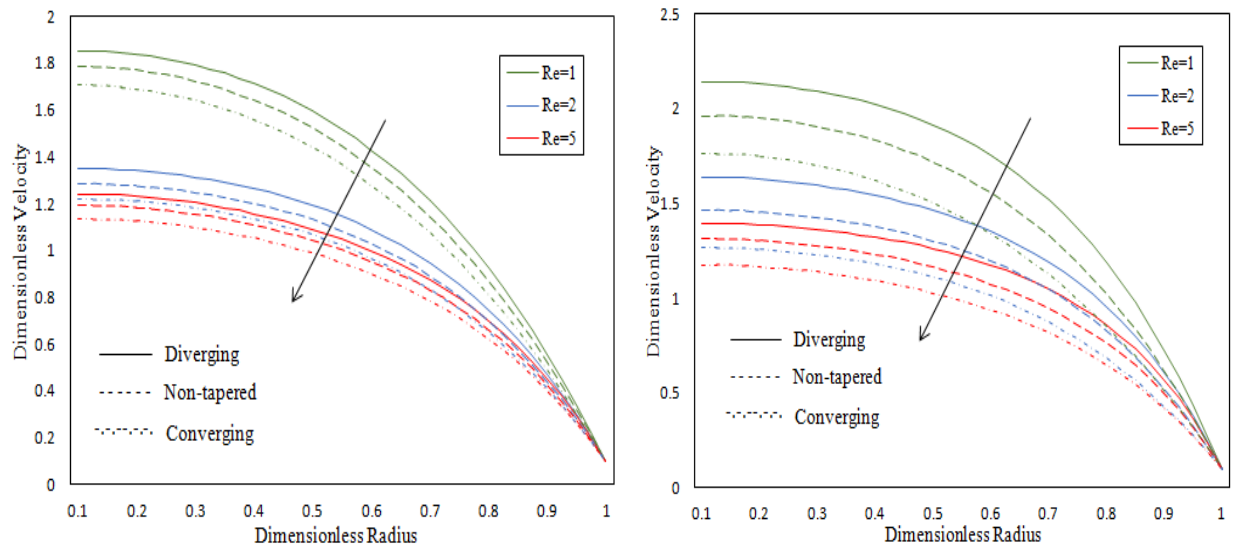


Figure 15: Effect of Reynolds number (Re) on axial velocity with $(Ag+Cu)$ hybrid nanofluid at (a) stenosis (b) aneurysm and $B_1 = 1.41, \delta = 0.1, t = 1.2$.

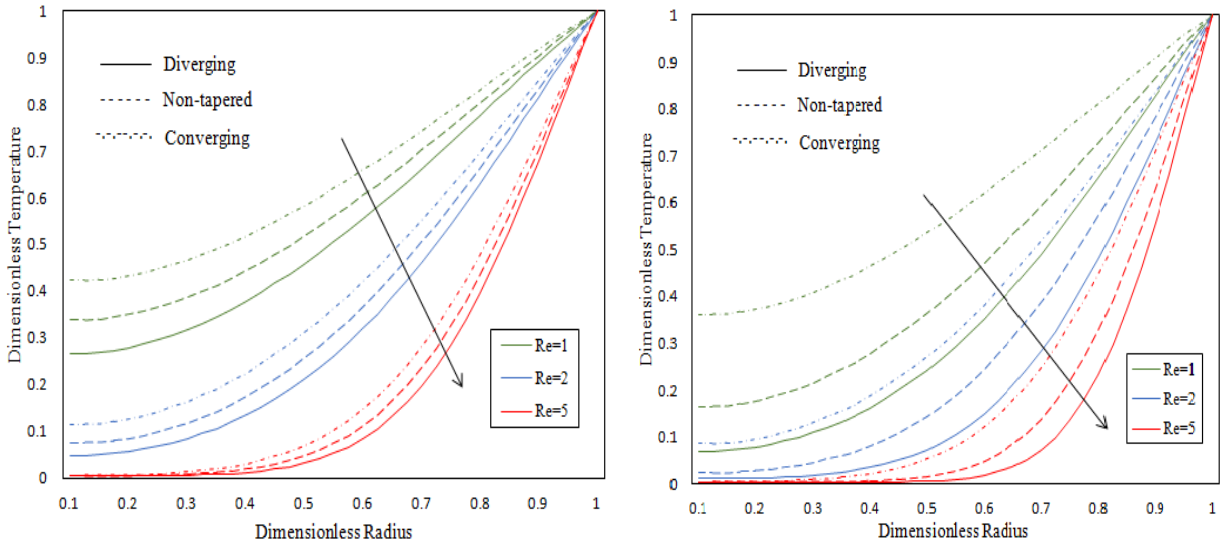


Figure 16: Effect of Reynolds number (Re) on temperature profile with $(Ag+Cu)$ hybrid nanofluid at (a) stenosis (b) aneurysm and $B_1 = 1.41, \delta = 0.1, t = 1.2$

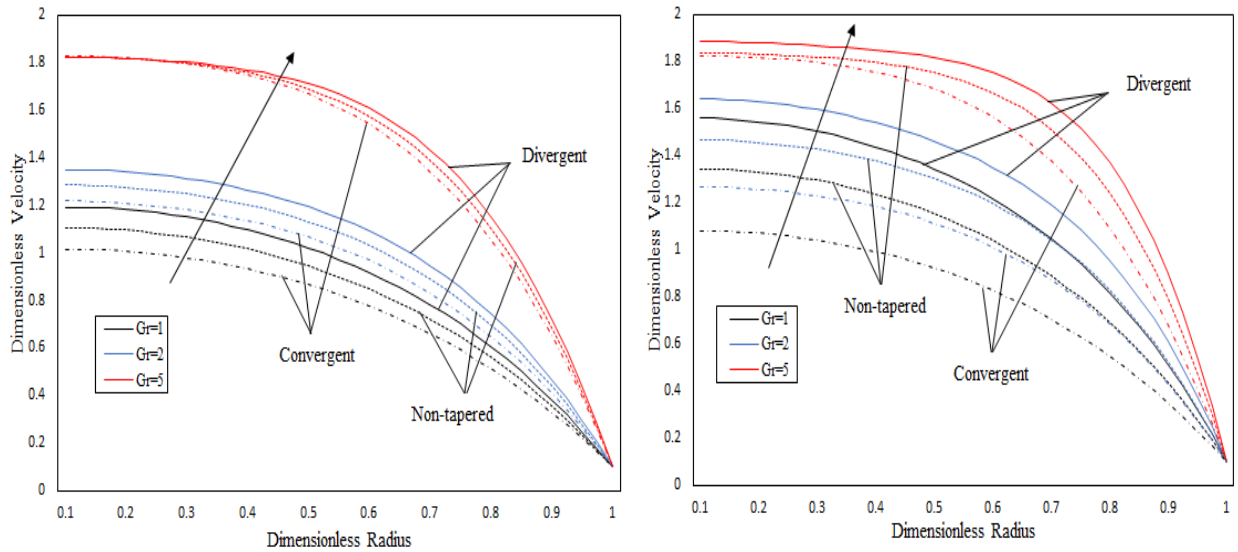


Figure 17: Effect of Grashof number (Gr) on axial velocity with $(Ag+Cu)$ hybrid nanofluid at (a) stenosis (b) aneurysm and $B_1 = 1.41, \delta = 0.1, t = 1.2$

The velocity profiles for variable Grashof numbers (Gr) (range 1-5) are plotted in **figure 17 (a)-(b)** for the stenosis and aneurysm regions, respectively. Grashof number (Gr) is the ratio of thermal buoyancy force to viscous force. Gravitational body force contributes to the thermal buoyancy force. There is also a concentration difference of nanoparticles within blood, although this does not produce a solutal (species) buoyancy force. The accentuation in thermal buoyancy encourages momentum diffusion and reduces impedance to the blood flow. This manifests in a concomitant

axial flow acceleration and elevation in axial velocity magnitudes. Evidently flow deceleration arises with weak thermal buoyancy force ($Gr = 1$) for which the thermal buoyancy force is equivalent to the viscous hydrodynamic force, as seen in figure 17 (a)-(b). Maximum axial flow velocity therefore is achieved with maximum Grashof number ($Gr = 5$). On comparing these two figures, it is also judicious to note that there is slightly higher velocity at the aneurysm region compared to the stenosis region.

The effect of various non-Newtonian parameters (m) (0.175-0.775) on axial velocity is given by **figure 18 (a)-(b)**. The parameter $m = \frac{\mu_{\infty}}{\mu_0}$, i.e. ratio of the dynamic viscosity (μ_0) and infinite

shear-rate viscosity (μ_{∞}) The graphs demonstrate that on increasing the value of m from 0.175 to 0.775, which corresponds to progressively stronger non-Newtonian flow (higher dynamic viscosity relative to the infinite shear-rate viscosity in the Carreau rheological model) a *strong deceleration* is computed at both (a) stenosis and (b) aneurysm. The velocity is always higher at aneurysm region for all the values of ‘ m ’ and *diverging tapered arteries* have maximum value in contrast to non-tapered and converging arteries. The rheological effect therefore produces a substantial modification in axial velocity distributions, which cannot be captured with classical Newtonian models.

The impact of Darcy number (\sqrt{Da}) (range 0.05-0.2) on velocity profile is given by **figure 19 (a)-(b)** at stenosis and aneurysm region, respectively. This parameter also features in the boundary condition (44) i.e. $\frac{\partial w}{\partial x} = \frac{\alpha}{\sqrt{Da}} [w_B - w_{porous}]$, and is used to quantify the permeability of the porous

wall of the artery. It is distinct from the porous parameter (α) which is associated with lateral mass flux alone. As we increased the Darcy number from 0.05 to 0.2, the axial velocity is also elevated by a significant amount since the permeability of the wall is increased permitting greater influx of blood. A greater magnitude of velocity is found for the *diverging artery at the aneurysm region* in comparison to the *non-tapered and converging artery cases* at the stenosis region of the artery.

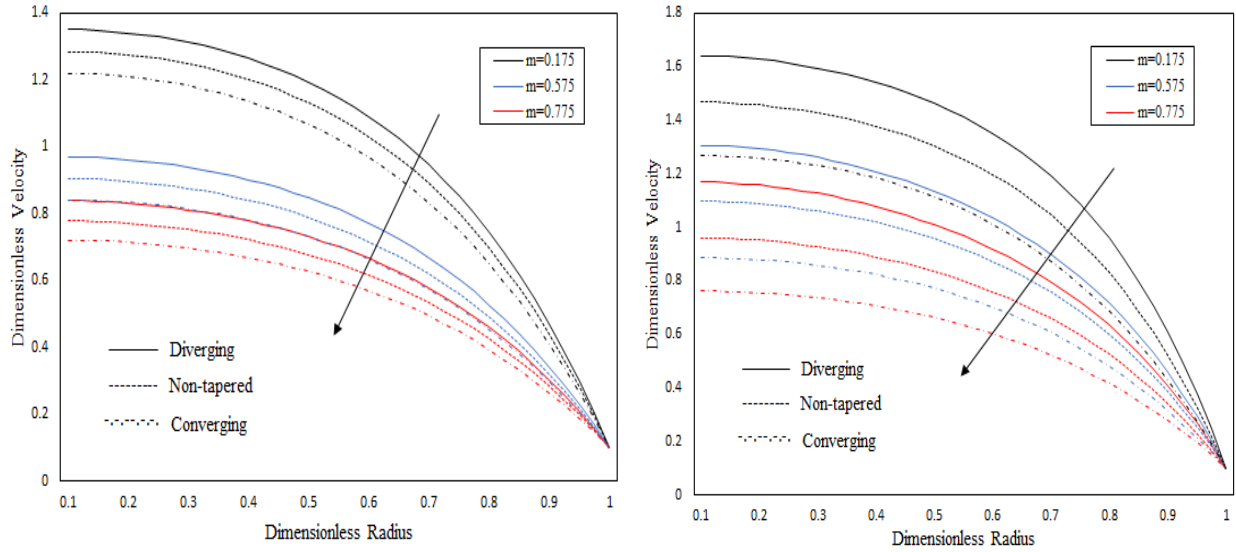


Figure 18: Effect of Non-newtonian parameter (m) on axial velocity with ($Ag+Cu$) hybrid nanofluid at (a) stenosis (b) aneurysm and $B_1 = 1.41, \delta = 0.1, t = 1.2$

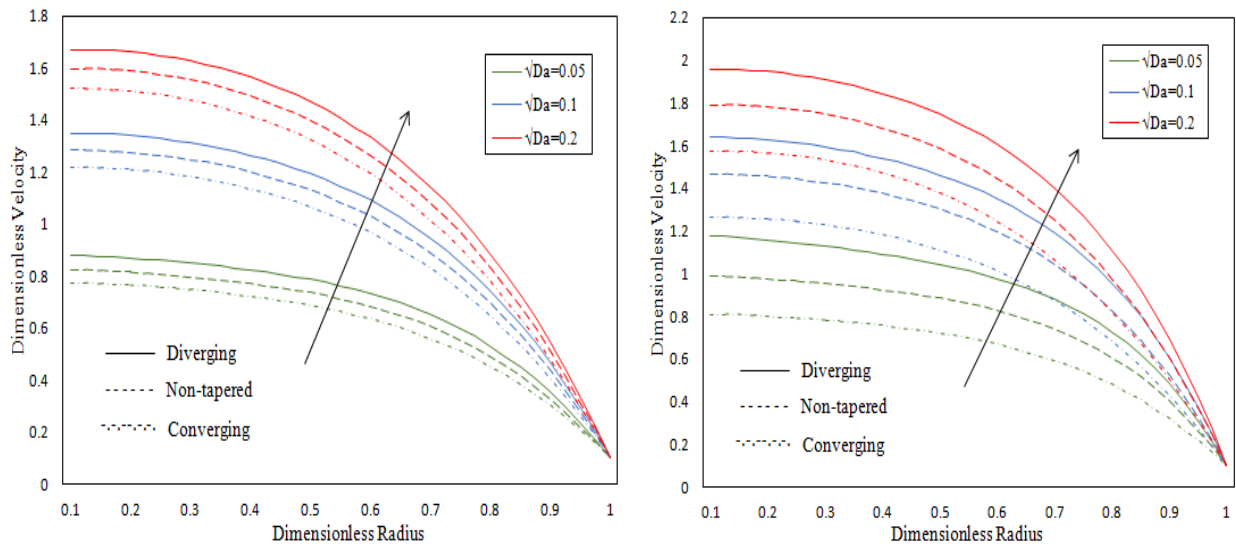


Figure 19: Effect of Darcy number (\sqrt{Da}) on axial velocity with ($Ag+Cu$) hybrid nanofluid at (a) stenosis (b) aneurysm and $B_1 = 1.41, \delta = 0.1, t = 1.2$

The impact of inclination angle (λ) of the artery on axial velocity profile is depicted in **figure 20 (a)-(b)**. The graphs reveal that on increasing the inclination angle from 0° to 90° , the velocity is boosted, and axial flow is accelerated significantly. This shows that for horizontal artery ($\lambda=0^\circ$) the velocity is minimal; however, with increment in inclination angle eventually to the *vertical artery case* ($\lambda=90^\circ$), the velocity achieves its maximum value. From both the figures, it is clear

that *diverging arteries* achieve higher values in comparison with converging and non-tapered arteries.

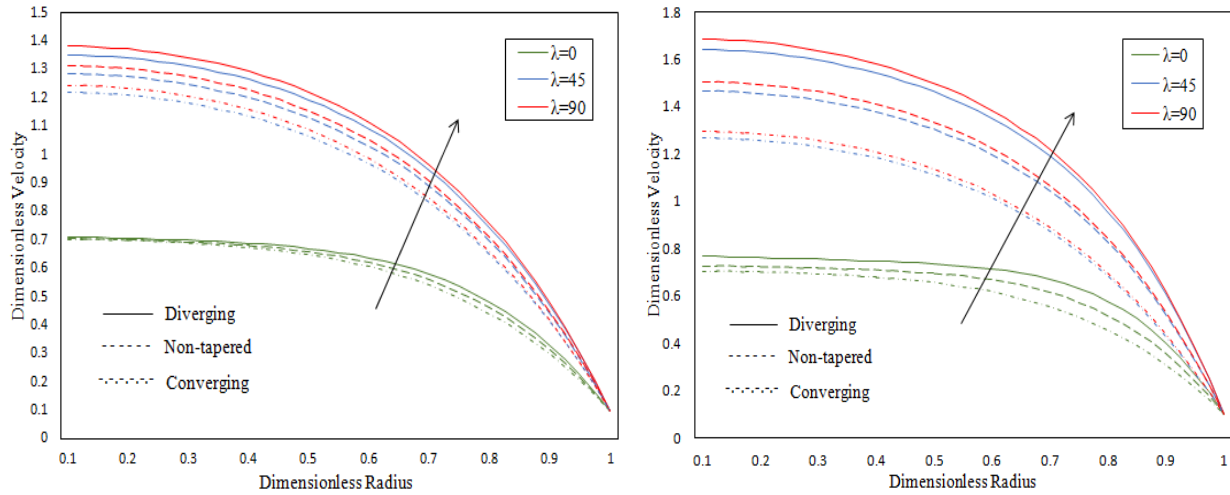


Figure 20: Effect of inclination angle (λ) on axial velocity with $(Ag+Cu)$ hybrid nanofluid at (a) stenosis (b) aneurysm and $B_1 = 1.41$, $\delta = 0.1$, $t = 1.2$

In **figure 21**, the influence of pressure gradient (pulsatile flow) parameter B_1 (featured in the non-dimensional form of pressure gradient) on velocity distribution for different tapering artery cases is visualized. For different sizes of artery, B_1 assumes different values. For example, with arterioles or the *coronary artery*, the value of B_1 is 1.41. However, for the femoral artery in the human body, B_1 attains a greater value of 6.6 – see Burton [42]. It is evident that on increasing the pressure parameter, the blood flow is significantly accelerated, confirming that femoral artery attains the maximum value and significantly exceeds the axial velocity computed for the coronary artery. Additionally, in aneurysm region, axial velocity is always higher compared to the stenosis region for all the tapering cases examined (i.e. diverging, non-tapered or converging).

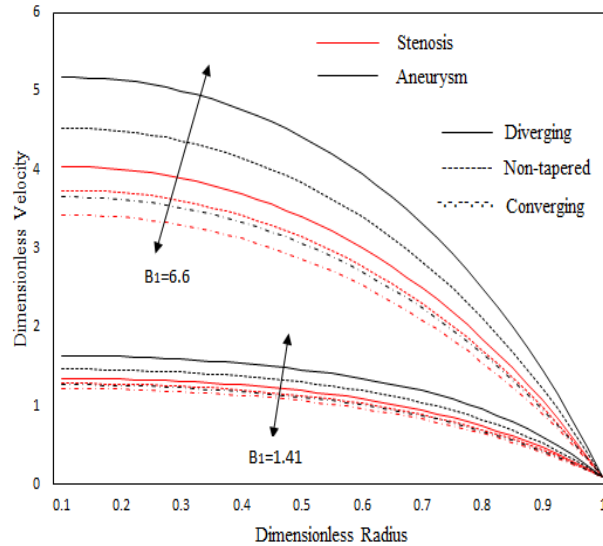


Figure 21: Effect of pressure parameter (B_1) on axial velocity with $(Ag+Cu)$ hybrid nanofluid at stenosis and aneurysm considering $\phi = 0.03$, $\delta = 0.1$, $t = 1.2$

The effects of hybrid nanoparticle volume fraction ($\phi_1+\phi_2$) on wall shear stress and volumetric flow rate profiles are presented in **figures 22-25**. **Figure 22-23** shows time series plots for wall shear stress (WSS) at the stenosis and aneurysm regions while **Figures 24-25** depict the volumetric flow rates at the stenosis and aneurysm, respectively. These figures capture the oscillatory nature of the blood flow in the stenotic region and allow a direct comparison between the performance at stenosis and aneurysm region with progression in time. Both figures for the wall shear stress show that the magnitude initially decreases and, after a critical point in time, then exhibits an ascending trend which is sustained with subsequent time. The graphs also indicate that with increasing magnitude of nanoparticle volume fractions, wall shear stress also *increases*. A minor difference is observed between the values of wall shear stress for diverging, converging and non-tapered arterial cases. Values computed at the aneurysm are consistently slightly in excess of those observed at the stenosis region.

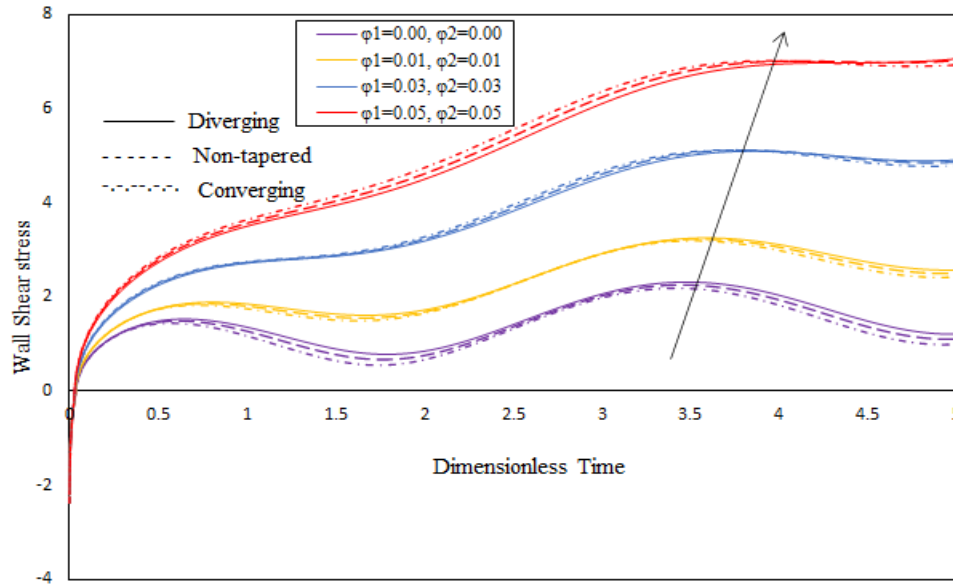


Figure 22: Effect of nanoparticle concentration (ϕ) on wall shear stress at stenosis for hybrid nanoparticles at $B_1 = 1.41, \delta = 0.1, z = 0.7$

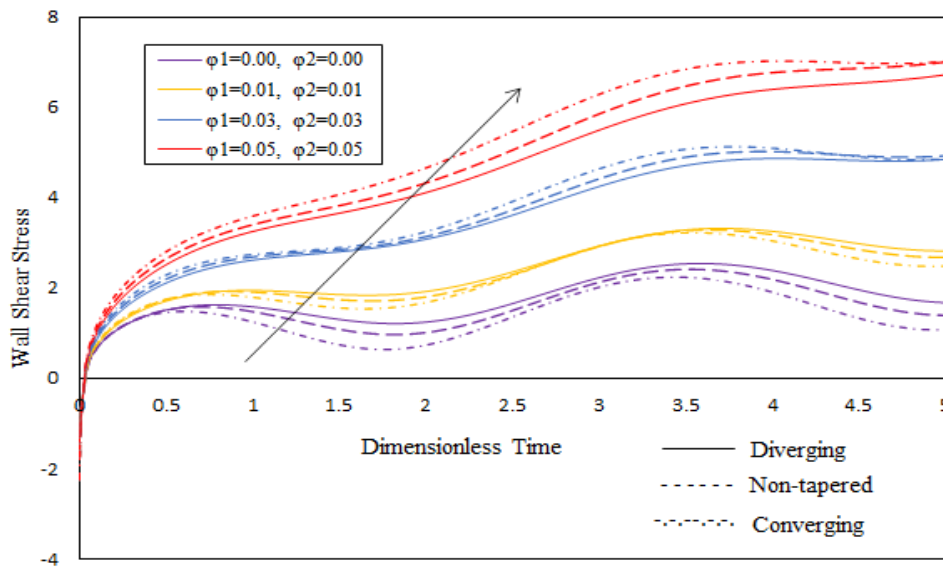


Figure 23: Effect of nanoparticle concentration (ϕ) on wall shear stress at aneurysm for hybrid nanoparticles at $B_1 = 1.41, \delta = 0.1, z = 2.2$

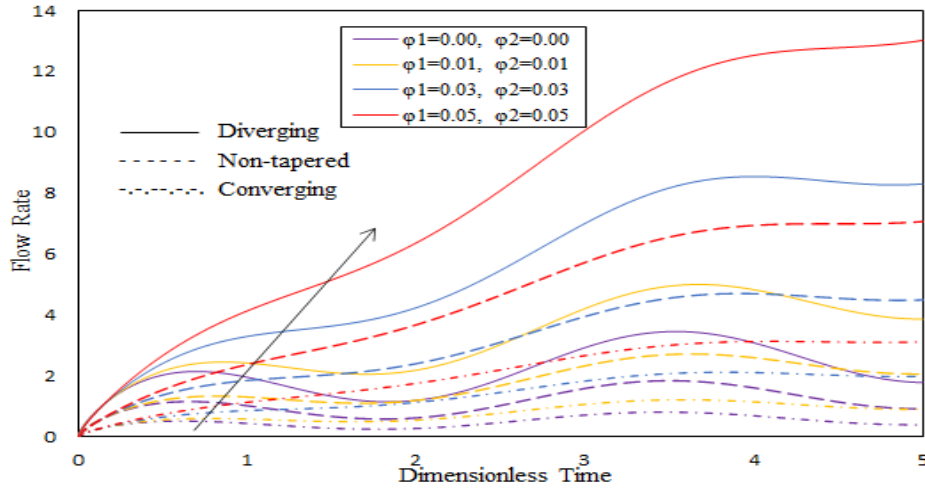


Figure 24: Effect of nanoparticle concentration (ϕ) on volumetric flow rate at stenosis for hybrid nanoparticles at $B_1 = 1.41, \delta = 0.1, z = 0.7$

Figures 24 and 25 portray the impact of various hybrid nanoparticle (silver, copper) volume fractions (ϕ_1, ϕ_2) on volumetric flow rate profiles at the stenosis and aneurysm region, respectively. This quantity also significantly decreases initially and thereafter increases with progressive elapse in time. The *diverging artery* case attains the highest volumetric flow rate, followed by the non-tapered case and then the converging artery case. A significant amount of difference is found between the values of flow rates at the stenosis and aneurysm regions; volumetric flow rate is higher for the aneurysm zone in comparison to the stenosis region.

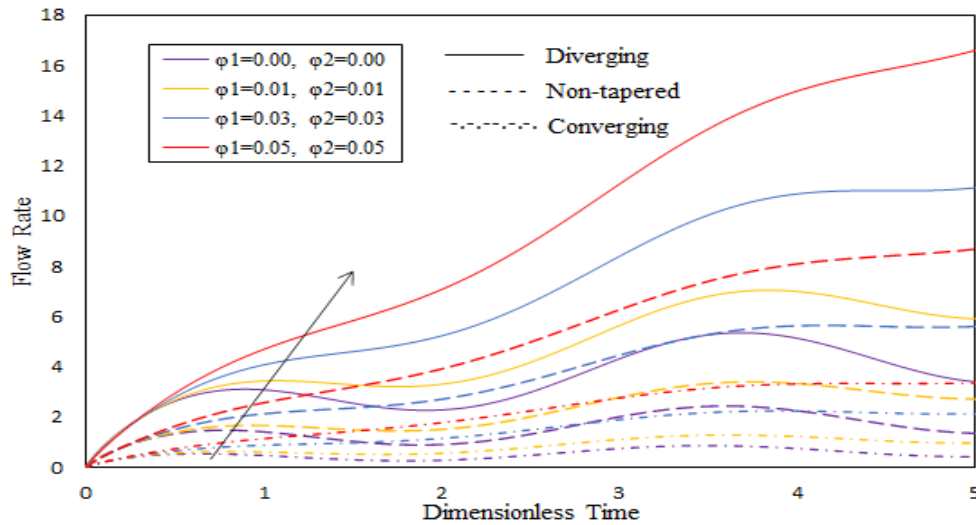


Figure 25: Effect of nanoparticle concentration (ϕ) on volumetric flow rate at aneurysm for hybrid nanoparticles at $B_1 = 1.41, \delta = 0.1, z = 2.2$

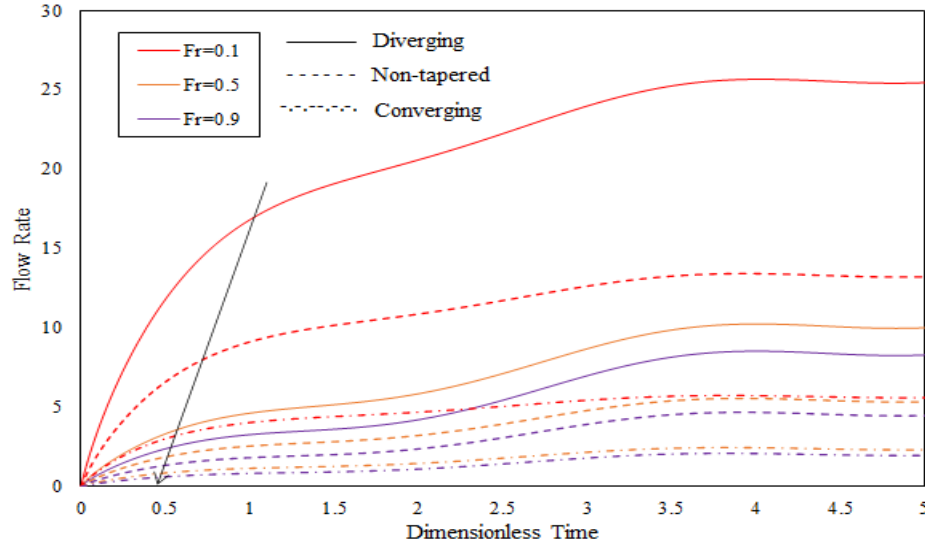


Figure 26: Effect of Froude parameter (Fr) on volumetric flow rate at stenosis for hybrid nanoparticles at $B_1 = 1.41, \delta = 0.1, z = 0.7$

The effect of Froude parameter (Fr) on volumetric flow rate at the stenosis and aneurysm regions is presented in **Figures 26-27**. On increasing the value of Fr from 0.1 to 0.9, flow rate is also decreased, following the same pattern of axial velocity profile, as computed earlier. Comparison between figures shows that diverging arteries have higher magnitudes of volumetric flow rate relative to non-tapered and converging cases. The value of volumetric flow rate is always lower in the stenosis region compared with the aneurysm region.

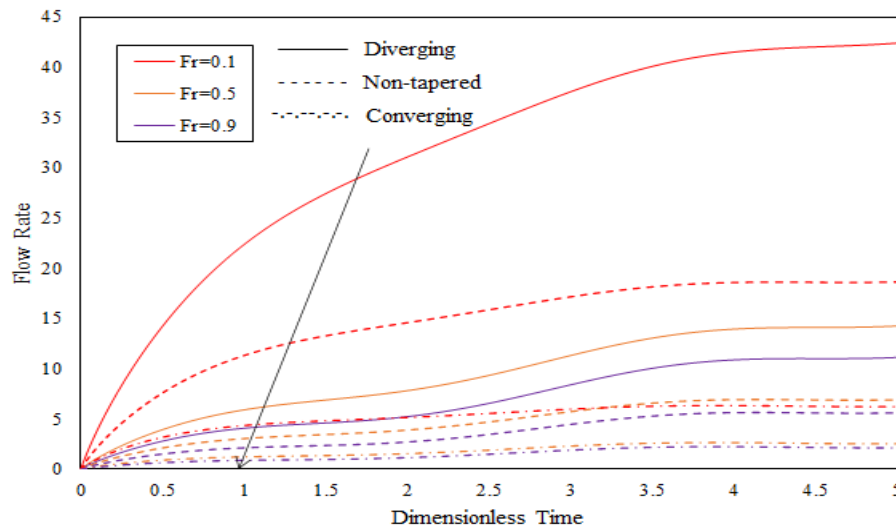


Figure 27: Effect of Froude parameter (Fr) on volumetric flow rate at aneurysm for hybrid nanoparticles at $B_1 = 1.41, \delta = 0.1, z = 2.2$

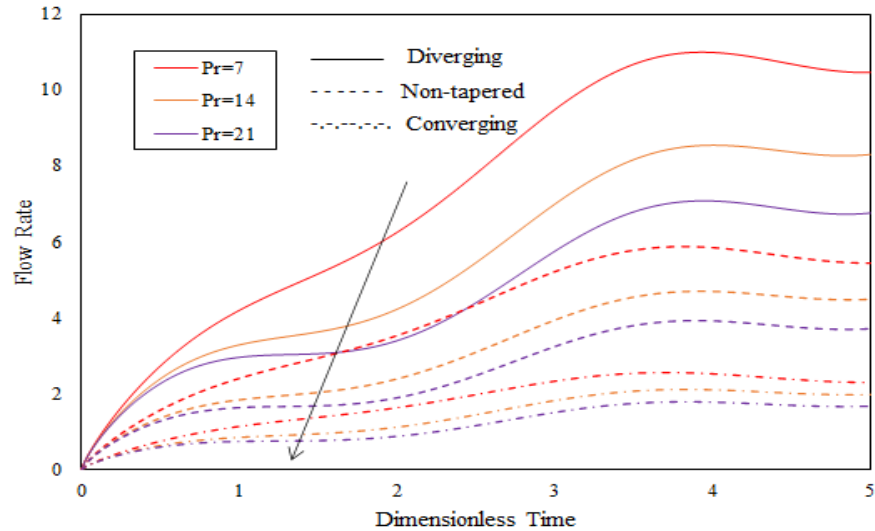


Figure 28: Effect of Prandtl number (Pr) on volumetric flow rate at *stenosis* for hybrid nanoparticles at $B_1 = 1.41, \delta = 0.1, z = 0.7$

Figure 28 and 29 illustrate the time-varying profile of volumetric flow rate for varying values of Prandtl number (Pr) at stenosis and aneurysm respectively. This quantity is diminished with elevation in Prandtl number from 7 to 21. There is again considerable difference between the values computed for tapered and non-tapered arteries; a maximum is attained for the diverging artery in both Figures 28 and 29. Volumetric flow rate values at the aneurysm region are comparatively higher than at the stenosis region.

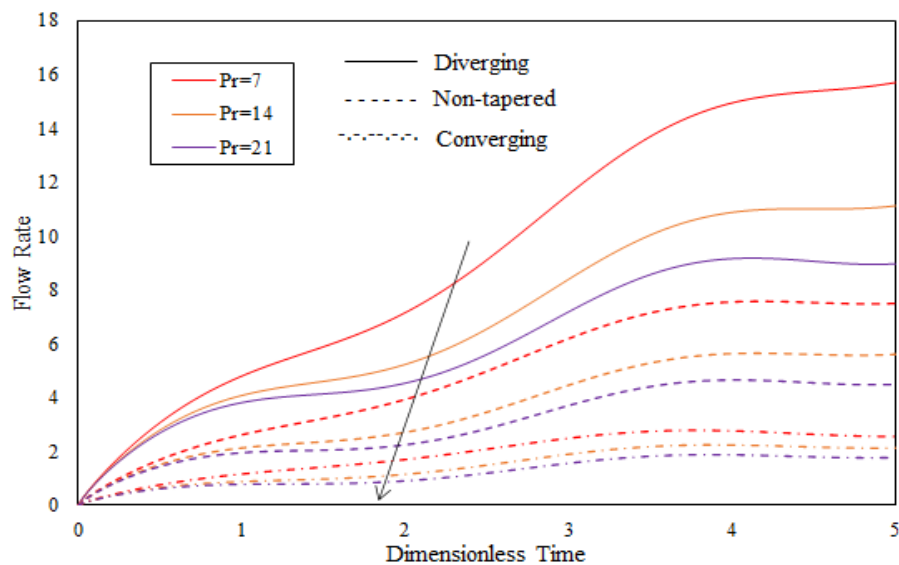


Figure 29: Effect of Prandtl number (Pr) on volumetric flow rate at *aneurysm* for hybrid nanoparticles at $B_1 = 1.41, \delta = 0.1, z = 2.2$

Figure 30 and 31 display the transient distributions for volumetric flow rates with increasing in Reynolds number (Re) and for different tapering artery scenarios. Strongly periodic profiles are again computed over a wide range of times. Generally, a consistent suppression in flow rate is observed with increasing the Reynolds number from 1 to 5, confirming the results computed earlier for axial velocity. As inertial effects are greater at higher Reynolds number, hence the dominant effect is flow retardation and decreased flux. Similar to the velocity profiles computed earlier, a diverging artery achieves a higher flow rate value compared to non-tapered and converging arteries.

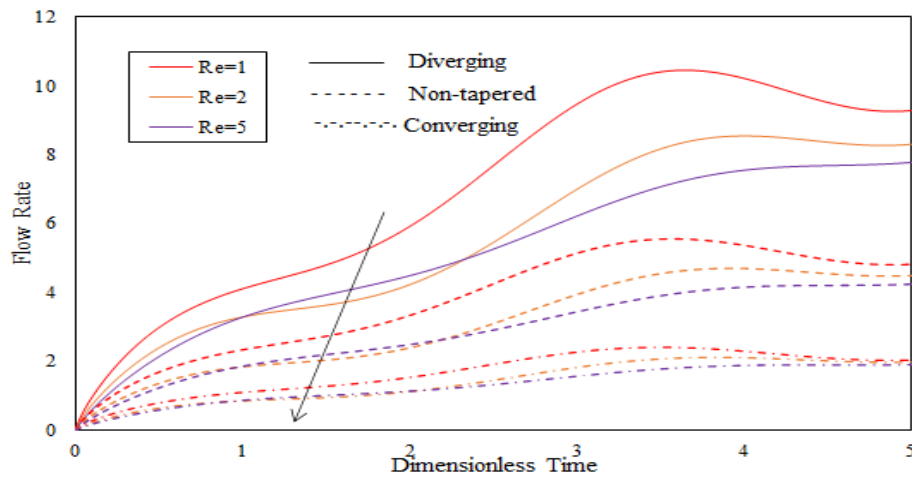


Figure 30: Effect of Reynolds number (Re) on volumetric flow rate at stenosis for hybrid nanoparticles at $B_1 = 1.41, \delta = 0.1, z = 0.7$

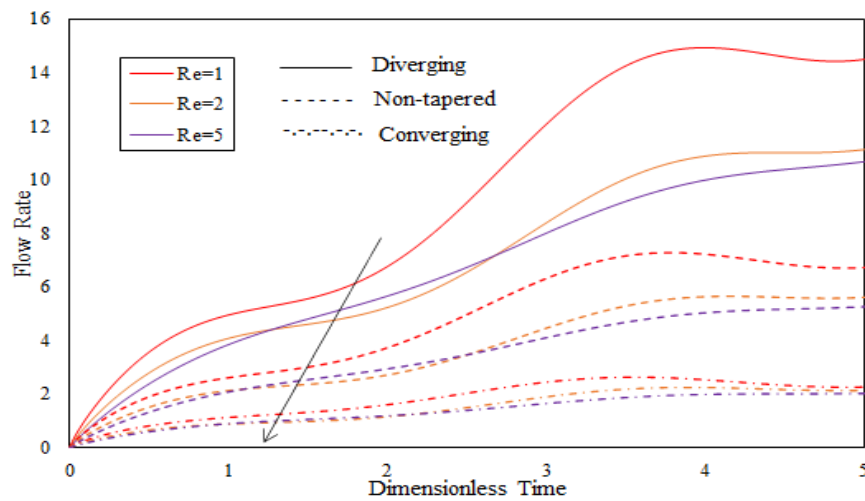


Figure 31: Effect of Reynolds number (Pr) on volumetric flow rate at aneurysm for hybrid nanoparticles at $B_1 = 1.41, \delta = 0.1, z = 2.2$

The impact of various nanoparticle shape factors on volumetric flow rate at stenosis and aneurysm is shown by **Figure 32-33**. Inspection of the graphs indicates that on increasing the shape factor from a minimum of 3.7 (bricks) to a maximum of 8.6 (blades), the flow rate is also elevated with time progression at both the stenosis and aneurysm locations. It is also seen that diverging arteries attain the highest magnitudes in comparison to non-tapered and converging arteries for any nanoparticle shape factor. On comparing both the figures, the maximum magnitude of flow rate is observed at the aneurysm section.

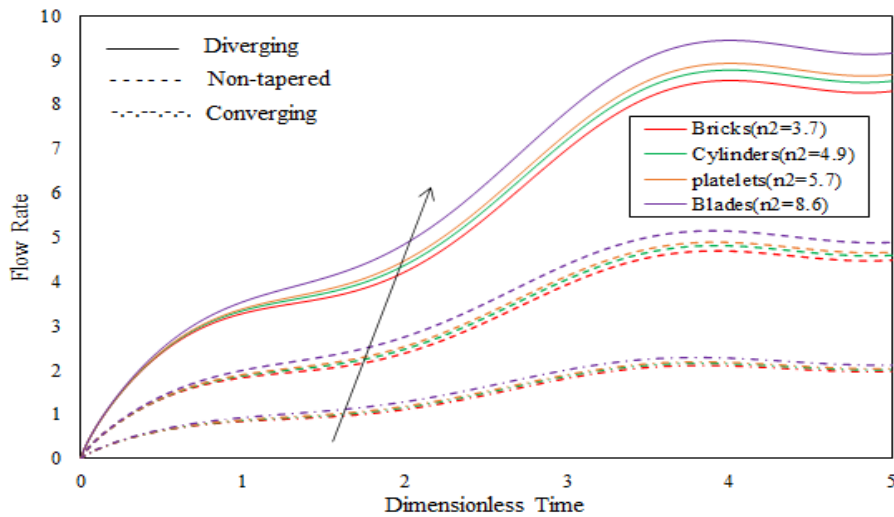


Figure 32: Effect of shape parameter (n_2) on volumetric flow rate at stenosis for hybrid nanoparticles at $B_1 = 1.41, \delta = 0.1, z = 0.7$

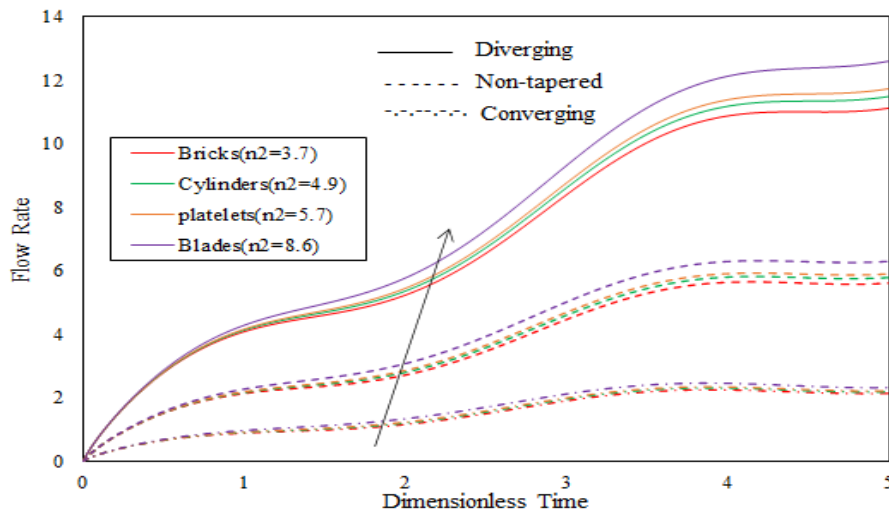


Figure 33: Effect of shape parameter (n_2) on volumetric flow rate at aneurysm for hybrid nanoparticles at $B_1 = 1.41, \delta = 0.1, z = 2.2$

Figure 34-35 display the influence of non-Newtonian parameter (m) on volumetric flow rate profile at stenosis and aneurysm segment respectively. The figures exhibit that on elevating the value of non-Newtonian parameter from 0.175 to 0.775, the flow rate shows a decrement i.e. the flow rate is reduced with increasing m . Strongly non-Newtonian flow ($m = 0.775$) therefore produces lower volumetric flow of blood compared with weaker non-Newtonian blood ($m = 0.175$) since dynamic viscosity in the former is much greater relative to the infinite shear rate viscosity. Diverging arteries achieve higher volumetric flow rate magnitudes compared to other cases (converging and non-tapered). Finally, it is pertinent to note that the flow rate values at the aneurysm segment are comparatively higher than at the stenosis segment.

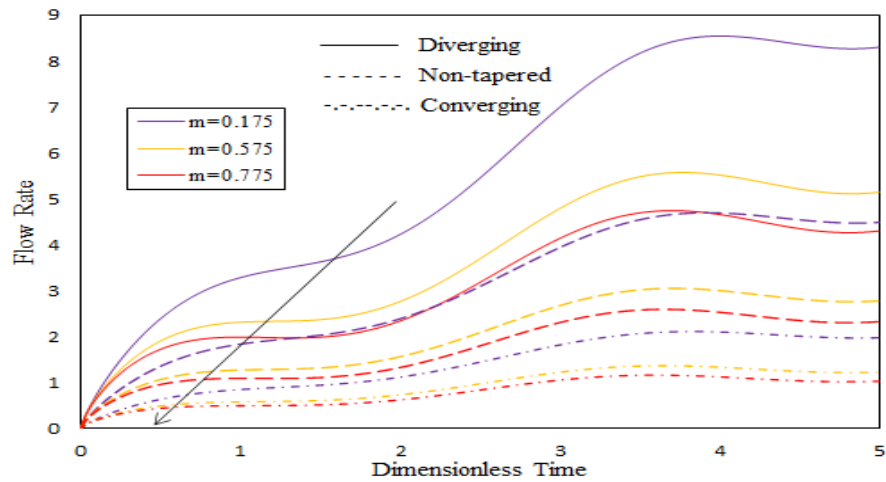


Figure 34: Effect of non-Newtonian parameter (m) on volumetric flow rate at stenosis for hybrid nanoparticles at $B_1 = 1.41, \delta = 0.1, z = 0.7$

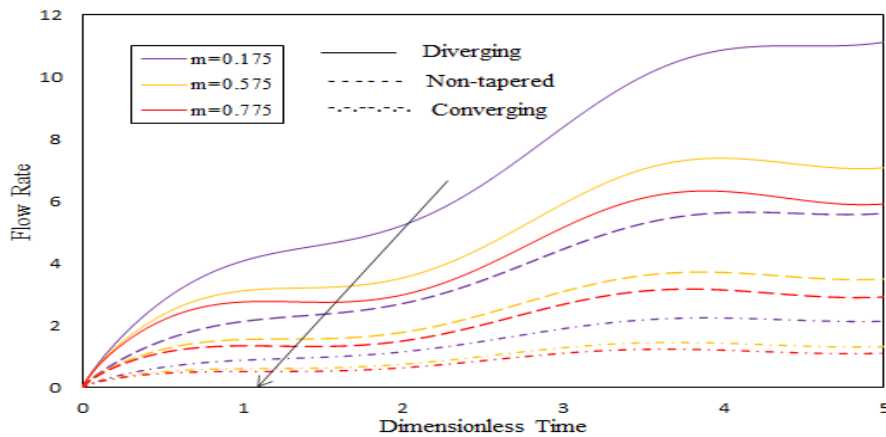


Figure 35: Effect of non-Newtonian parameter (m) on volumetric flow rate at aneurysm for hybrid nanoparticles at $B_1 = 1.41, \delta = 0.1, z = 2.2$

8. Conclusions:

Inspired by nano-drug delivery technologies for the treatment of arterial diseases, this study describes a *theoretical and computational simulation of unsteady hybrid-nanoparticle (silver and copper) hemodynamics in inclined, catheterized diseased arteries with mild stenosis aneurysm features*. A tapering geometry (converging and diverging), arterial wall permeability, and wall slip are considered to simulate the blood flow characteristics in arterial transport more accurately. Heat generation and thermal buoyancy effects are also included. To mimic the non-Newtonian characteristics of blood (hemorheology), the Carreau fluid model is taken into account. For realistic flow situations, the unsteady component of the pulsatile pressure gradient is included. Various shaped nanoparticles, i.e., bricks, cylinders, platelets, blades, are studied. The transformed nonlinear conservation equations with initial and boundary conditions are solved with realistic data using a finite difference method (FTCS). Extensive graphical plots for the impact of emerging parameters on hemodynamic characteristics (velocity, temperature, wall shear stress, and volumetric flow rate) at both the stenosis and aneurysm segments are computed. Validation with previous studies is also conducted. The key conclusions from the present numerical computations are summarized as follows:

- The inclusion of hybrid nanoparticles (Ag-Cu/Blood) within blood increases the axial velocity and temperature magnitudes more significantly as compared to unitary nanoparticles (Ag/blood) at both the stenosis and aneurysm segments.
- With an increment in nanoparticle shape factor (n_2), axial velocity, temperature and flow rate are all enhanced.
- On increasing the slip velocity (w_b) and Froude number (Fr), axial velocity decreases at both stenosis and aneurysm segments.
- Increment in Darcy number (Da) (wall permeability parameter) induces blood flow acceleration whereas an increment in porous parameter (α) decreases the velocity.
- The axial velocity of blood increases with greater Grashof number (Gr) while axial flow deceleration and temperature depletion is generated with increasing Reynolds number (Re) and Prandtl number (Pr).
- Increment in heat generation parameter (β) produces strong elevation in axial velocity and temperature, both at the stenosis and aneurysm diseased segments.

- With increment in arterial inclination angle (λ), velocity is also increased, and the highest axial velocity is obtained for the vertical artery case.
- Axial velocity is always a maximum for the *diverging artery* compared to the non-tapered and converging artery cases. Conversely, magnitudes of temperature are highest for the converging artery relative to the diverging and non-tapered cases.
- Magnitude of velocity, temperature, wall shear stress and volumetric flow rate profiles are always comparatively higher at the aneurysm region compared with the stenosis segment.

The present simulations have revealed some interesting insights into non-Newtonian hybrid nano-doped blood flow through a catheterized artery featuring both stenosis and aneurysm. Percutaneous coronary intervention (PCI) has become the most common revascularization procedure for coronary artery disease [49]. The use of stents has reduced the rate of restenosis by preventing elastic recoil and adverse remodeling. *Electrokinetic viscoelastic* blood flows [50] are also of great interest in nano-pharmacodynamics. Furthermore, Taylor dispersion is also of great relevance as are chemical reaction effects in oxygen diffusing through rheological blood [51]. Future studies will be orientated in these directions and may include arterial wall deformability (fluid-structure interaction).

Acknowledgements

The authors are grateful to the Science and Engineering Research Board (SERB), Department of Science and Technology (DST), Government of India for undertaking the research work under the research project *File Number: ECR/2017/001053* dated 12/03/2018.

References:

1. E. Rindfleish, Manual of Pathological Histology. New Sydenham Soc, London, 250 (1) (1972) 137–143.
2. M. Nazemi, C. Kleinstreuer, J. P. Archie, F. Y. Sorrell, Fluid flow and plaque formation in an aortic bifurcation. ASME J Biomech Eng (111) (1989) 316-324.
3. D. L. Fry, Responses of the arterial wall to certain physical factors. Atherogenesis: Initiating Factors. Association of Scientific publishers, Amsterdam (12) (1973) 93-125.
4. V. Deplano, C. Bertolotti, O. Boiron, Numerical simulations of unsteady flows in a stenosed coronary bypass graft. Med Biol Eng Comput, 39 (4) (2001) 488-499.
5. D. S. Sankar, Two-phase non-linear model for blood flow in asymmetric and axisymmetric stenosed arteries. Int J Non Linear Mech, 46 (1) (2011) 296-305.
6. T. K. Hung, T. M. C. Tsai, Kinematic and dynamic characteristics of pulsatile flows in stenotic vessels. ASCE J Eng Mech, 123 (3) (1997) 247-259.

7. N. Srivastava, Analysis of flow characteristics of the blood flowing through an inclined tapered porous artery with mild stenosis under the influence of an inclined magnetic field. *J Biophys*, (2014) 797142.
8. S. Chakravarty, P. K. Mandal, Mathematical modelling of blood flow through an overlapping arterial stenosis. *Math Comput Model*, 19 (1) (1994) 59-70.
9. N. Mustapha, N. Amin, S. Chakravarty, P. K. Mandal, Unsteady magnetohydrodynamic blood flow through irregular multi-stenosed arteries. *Comput Biol Med*, 39(10) (2009) 896-906.
10. K. K. L. Wong, J. Tu, J. Mazumdar, D. Abbott, Modelling of blood flow resistance for an atherosclerotic artery with multiple stenoses and post-stenotic dilatations. *ANZIAM J*, 51 (2009) C66-C82.
11. K. L. Moore, A. F. Dalley, Clinically oriented anatomy. Wolters kluwer india Pvt Ltd (2018).
12. F. J. Gijsen, E. Allanic, F. N. Van De Vosse, J. D. Janssen, The influence of the non-Newtonian properties of blood on the flow in large arteries: unsteady flow in a 90 curved tube. *J Biomech*, 32 (1999) 705-13.
13. R. Manica, A. L. De Bortoli, Simulation of sudden expansion flows for power-law fluids. *J Non-Newton Fluid Mech*, 121 (2004) 35-40.
14. B. Pincombe, J. Mazumdar, The effects of post-stenotic dilatations on the flow of a blood analogue through stenosed coronary arteries. *Math Comput Model*, 25(6), (1997) 57-70.
15. N. Ali, A. Zaman, O. Anwar Bég, M. Sajid, Unsteady two-layer blood flow through a w-shape stenosed artery using the generalized Oldroyd-B fluid model, *ANZIAM J*, 58, (2016) 1-23.
16. N. Ali, A. Zaman and O. Anwar Bég, Numerical simulation of unsteady micropolar hemodynamics in a tapered catheterized artery with a combination of stenosis and aneurysm, *Med Biol Eng Comput*, 54, (2016) 1423–1436.
17. J. Bernsdorf, D. Wang, Non-Newtonian blood flow simulation in cerebral aneurysms. *Comput Math with Appl*, 58(5), (2009) 1024-1029.
18. A. R. Mantha, G. Benndorf, A. Hernandez, R. W. Metcalfe, Stability of pulsatile blood flow at the ostium of cerebral aneurysms. *J. Biomech*, 42(8), (2009) 1081-1087.
19. M. Sharzehee, S. S. Khalafvand, H. C. Han, Fluid-structure interaction modeling of aneurysmal arteries under steady-state and pulsatile blood flow: A stability analysis. *Comput Methods Biomech Biomed Engin*, 21(3), (2018) 219-231.
20. V. P. Srivastava, R. Rastogi, Blood flow through a stenosed catheterized artery: Effects of hematocrit and stenosis shape. *Comput Math with Appl*, 59(4), (2010) 1377-1385.
21. K. S. Mekheimer, A. Z. Zaher, A. I. Abdellateef, Entropy hemodynamics particle-fluid suspension model through eccentric catheterization for time-variant stenotic arterial wall: Catheter injection. *Int J Geom Methods Mod Phys*, 16(11), (2019) 1950164.
22. A. Ahmed, S. Nadeem, Shape effect of Cu-nanoparticles in unsteady flow through curved artery with catheterized stenosis. *Results Phys*, 7, (2017) 677-689.
23. R. Bali, U. Awasthi, Mathematical model of blood flow in small blood vessel in the presence of magnetic field. *Appl Math.*, 2, (2011) 264-9.
24. R. K. Srivastav, Mathematical model of blood flow through a composite stenosis in catheterized artery with permeable wall. *Appl Math.*, 9, (2014) 58-74.
25. R. Singh, G. C. Sharma, M. Jain, Mathematical modeling of blood flow in a stenosed artery under MHD effect through porous medium. *Int J Eng Trans B: Appl*, (2010): 23, 243-52.
26. N. S. Akbar, D. Tripathi, O. Anwar Bég, Variable-viscosity thermal hemodynamic slip flow conveying nanoparticles through a permeable-walled composite stenosed artery, *Eur Phys J Plus*, 132, (2017) 294 -305.
27. I. M. Eldesoky, Slip effects on the unsteady MHD pulsatile blood flow through porous medium in an artery under the effect of body acceleration. *Int J Math Math Sci*, (2012) 860239.
28. S U Choi, J A Eastman, Enhancing thermal conductivity of fluids with nanoparticles. Argonne National Lab., IL (United States) (1995).
29. J. Tripathi, B. Vasu, A. Dubey, R.S. Gorla, P.V. Murthy, O. Anwar Bég, V.R Prasad, P. Saikrishnan, A review on recent advancements in the hemodynamics of nano-drug delivery systems. *NanoSci Technol* 11: (2020) 73-98.

30. B. Vasu, A. Dubey, O. Anwar Bég, Finite element analysis of non-Newtonian magneto-hemodynamic flow conveying nanoparticles through a stenosed coronary artery. *Heat Tran Asian Res.* 49, (2020) 33-66.
31. N Ali, A. Zaman, M. Sajid, O. Anwar Bég, M.D. Shamsuddin, A. Kadir, Numerical simulation of time-dependent non-Newtonian nano-pharmacodynamic transport phenomena in a tapered overlapping stenosed artery. *NanoSci Technol: An Int. J* (2018): 9:2.
32. S. Nadeem, S. Ijaz, Theoretical analysis of metallic nanoparticles on blood flow through stenosed artery with permeable walls. *Phys Lett A*, 379, (2015) 542-54.
33. A. Ahmed, S. Nadeem, The study of (Cu, TiO₂, Al₂O₃) nanoparticles as antimicrobials of blood flow through diseased arteries. *J Mol Liq.* 216, (2016) 615-23.
34. A. Makishima, Possibility of hybrid materials. *Ceram. Jap.*, 39(2), (2004) 90-91.
35. J. Tripathi, B. Vasu, O. Anwar Bég, Computational simulations of hybrid mediated nano-hemodynamics (Ag-Au/Blood) through an irregular symmetric stenosis. *Comput Biol Med*, 130, (2021) 104213.
36. A. Zaman, N. Ali, I. Ali, Effects of nanoparticles (Cu (Copper), Silver (Ag)) and slip on unsteady blood flow through a curved stenosed channel with aneurysm. *Therm Sci Eng Prog.* 5, (2018) 482-491.
37. J. Tripathi, B. Vasu, O. Anwar Bég, R. S. R. Gorla, Unsteady hybrid nanoparticle-mediated magneto-hemodynamics and heat transfer through an overlapped stenotic artery: Biomedical drug delivery simulation. *Proc Inst Mech Eng H*, 09544119211026095, (2021)
38. S. Nadeem, S. Ijaz, Influence of metallic nanoparticles on blood flow through arteries having both stenosis and aneurysm. *IEEE Trans Nanobiosci*, 14(6), (2015) 668-679.
39. A. Zaman, N. Ali, A. A. Khan, Computational biomedical simulations of hybrid nanoparticles on unsteady blood hemodynamics in a stenotic artery. *Math Comput Simul*, 169, (2020) 117-132.
40. A. Zaman, A. A. Khan, N. Ali, Modeling of unsteady non-Newtonian blood flow through a stenosed artery: with nanoparticles. *J Braz Soc Mech Sci Eng*, 40(6), (2018) 1-12.
41. S. A. Devi, S. S. U. Devi, Numerical investigation of hydromagnetic hybrid Cu–Al₂O₃/water nanofluid flow over a permeable stretching sheet with suction. *Int J Nonlinear Sci Numer Simul*, 17(5), (2016) 249-257.
42. A. C. Burton, Introductory text, *Physiology and Biophysics of the Circulation*. Year Book Medical Publisher, Chicago, IL (1966).
43. K. A. Hoffmann, S.T. Chiang, *Computational Fluid Dynamics*. Vol. 1. Wichita, KS: Engineering Education System, p.486.
44. S. Ijaz, S. Nadeem, Examination of nanoparticles as a drug carrier on blood flow through catheterized composite stenosed artery with permeable walls. *Comput Methods Programs Biomed.* 133, (2016) 83-94.
45. V. Mitvalský, Heat transfer in the laminar flow of human blood through tube and annulus. *Nature*, 206(4981), (1965) 307-307.
46. K. R. Diller, Fundamentals of Bioheat Transfer. In *Physics of Thermal Therapy* (20-39). (2016) CRC Press.
47. D. W. Hensley, A. E. Mark, J. R. Abella, G. M. Netscher, E. H. Wissler, K. R. Diller, 50 years of computer simulation of the human thermoregulatory system. *ASME J. Biomech Eng*, 135(2) (2013).
48. N. S. Akbar, A. W. Butt, Magnetic field effects for copper suspended nanofluid venture through a composite stenosed arteries with permeable wall. *J Magn Magn Mater*, 381, (2015) 285-291.
49. R. X. Yin, D. Z. Yang, J. Z. Wu, Nanoparticle drug-and gene-eluting stents for the prevention and treatment of coronary restenosis. *Theranostics*, 4(2), (2014) 175.
50. D. Tripathi, A. Sharma, O. Anwar Bég, A. Tiwari. Electrothermal transport in biological systems: an analytical approach for electrokinetically modulated peristaltic flow. *J Therm Sci Eng Appl*; (2017) 9:041010.
51. A. K. Roy, O. Anwar Bég. Mathematical modelling of unsteady solute dispersion in two-fluid (micropolar-Newtonian) blood flow with bulk reaction. *Int Commun Heat Mass Transf*;122: (2021)105169.
52. S. Ijaz, S. Nadeem. Biomedical theoretical investigation of blood mediated nanoparticles (Ag-Al₂O₃/blood) impact on hemodynamics of overlapped stenotic artery. *J Mol Liq*, 248, (2017) 809-821.